Inaugural Dissertation
zur Erlagerung des Doktorgrades
der Naturwissenschaften
der Justus-Liebig Universität Gießen
(Fachbereich Physik)

First mass measurements of stored and cooled neutron-rich ^{238}U projectile fragments in the element range of $87 \leq Z \leq 92$ at the FRS-ESR Facility

vorgelegt von
Evangelia Kaza
geboren in Athen

Juli 2004

Προσπάθησε να οδηγήσεις την τεχνική τελειότητα στη φυσική της κατάσταση

Φτασμένες οι προλήψεις σε μια καθαρότητα μαθηματική θα μας βοηθούσανε να κατανοήσουμε τη βαθύτερη δομή του κόσμου

Οδυσσέας Ελύτης, ΣΗΜΑΤΟΛΟΓΙΟΝ

Zusammenfassung

Experimentelle Daten über die Struktur der neutronreichen Kerne zwischen Blei und Uran sind nur spärlich vorhanden. Zur Produktion dieser exotischen Kerne wurde ein Uranstrahl auf einem Berylliumtarget fragmentiert. Die produzierten Sekundärteilchen wurden mit Hilfe des Fragmentseparators FRS im Fluge nach ihrer magnetischen Steifigkeit separiert und in den Experimentierspeicherring ESR eingeschossen. Dort wurden sie gespeichert und mit Hilfe des Elektronenkühlers alle auf die gleiche Geschwindigkeit gebracht. Ihre Umlauffrequenzen wurden kontinuierlich mit Hilfe von Schottky Massenspektrometrie bestimmt.
Das für diese Messung entwickelte und zum ersten Mal angewendete Datenaufnahmesystem erlaubte eine effektive Handhabung der Daten; sämtliche wichtigen Parameter wurden online aufgezeichnet. Weiterhin konnte die Qualität der Messung in ihrem Verlauf genauestens überprüft werden. Um Daten über die Umlauffrequenz der Ionen zu erhalten, müssen die aufgenommenen Zeitmarken einer diskreten Fouriertransformation (FFT) unterzogen werden. Die daraus entstehenden Schottkyrauschdichtenspektren wurden hinsichtlich Frequenzauflösung und Signalrauschverhältnis optimiert. Weitere Verbesserungsvorschläge für das Datenaufnahmesystem konnten bei der Analyse dieser Daten gewonnen werden.
Mit Hilfe von Simulationspektren mit den gleichen Parametern wie im Experiment, konnte die Identifikation der Frequenzmarken durchgeführt werden. Die Massen der Isotope in allen aufgenommenen Spektren wurden mit einer Korrelationsmatrix bestimmt. Insgesamt wurden 23 Massen von Isotopen ermittelt von denen drei Massen zuvor nicht bekannt waren. Diese drei erstmalig gemessen Massen wurden mit modernen Massentheorien verglichen. Schließlich wurde die Möglichkeit untersucht, anhand von $^{233}\mathrm{Ac}^{88+}$ Halbwertszeitmessungen mit dem neuen Datenaufnahmesystem durchzuführen.

Summary

Experimental nuclear structure information about neutron-rich nuclei in the region between Pb and U is scarce. Projectile fragmentation of an U beam was applied to produce these exotic nuclei. The ions emerging from the target were separated in-flight in the fragment separator FRS and subsequently stored and electron-cooled to the same velocity in the Experimental Storage Ring ESR. Their revolution frequency in the ring was measured continuously by means of Schottky mass spectrometry.

The data acquisition system, which was developed and applied for the first time, offered an effective handling of the large data flow and recorded automatically the current experimental parameters. Furthermore, it allowed for on-line inspection of the recording, thus securing the quality of the measurement. In order to retrieve the information about the ions' circulation in the ring, the raw data were subjected to a Fast Fourier Transform. The parameters of the resulting Schottky noise power density spectra were selected such as to optimize the frequency resolution and the signal-to-noise ratio. By examining the performance of the new data acquisition system suggestions for its further improvement are made.

Calibrating the acquired frequency spectra, taking into account simulations of the experiment, provided the identification of their frequency peaks. Combining the assigned mass-to-charge ratios of the identified peaks of all the analyzed spectra in a correlation matrix yielded the mass values of the encountered nuclides. The masses of 23 different nuclides were obtained by our analysis, 3 of which for the first time. The newly measured masses were compared with modern mass theories. The feasibility of half-life measurements with the new data acquisition system was studied by determining the half-life of $^{233}\mathrm{Ac}^{88+}$.

Contents

1 Introduction 1

2 Experiment 3
2.1 Experimental setup 3
2.1.1 Fragment production and in-flight separation with the FRS 3
2.1.2 Ion injection, storage and cooling in the ESR 4
2.2 Schottky mass spectrometry 8
2.3 Frequency measurements 9

3 Data acquisition system 11

4 Data analysis 16
4.1 Data handling 16
4.1.1 Raw data information extraction 16
4.1.2 Creation of Schottky noise spectra 16
4.1.3 Optimization of spectral parameters 19
4.1.4 Comparison to relevant Schottky experiments 21
4.2 Spectrum analysis 23
4.2.1 Peak identification 25
4.2.2 Mass determination 28
4.3 Estimation of systematic error 29

5 Results 32
5.1 Comparison with theoretical predictions 33
5.2 Half-life measurement 36

Chapter 1

Introduction

The mass of a nucleus is one of its basic properties which reflects the complex interactions of all nucleons. Nuclear masses are essential to derive the information about the stability and the decay properties of nuclei, the borders of nuclear existence, the shell structure, changes in deformation and pairing [1]. Moreover nuclear masses are needed to determine the pathways of the astrophysical nucleosynthesis processes.

The present knowledge of nuclear masses is illustrated in Fig. 1.1. It is evident from this figure that the knowledge of masses for neutron-rich nuclei around uranium is very limited. Moreover only very few neutron-rich isotopes of these elements were observed in the laboratory so far, a fact that is caused by the difficulties in their production. This lack of experimental data is crucial for ad-

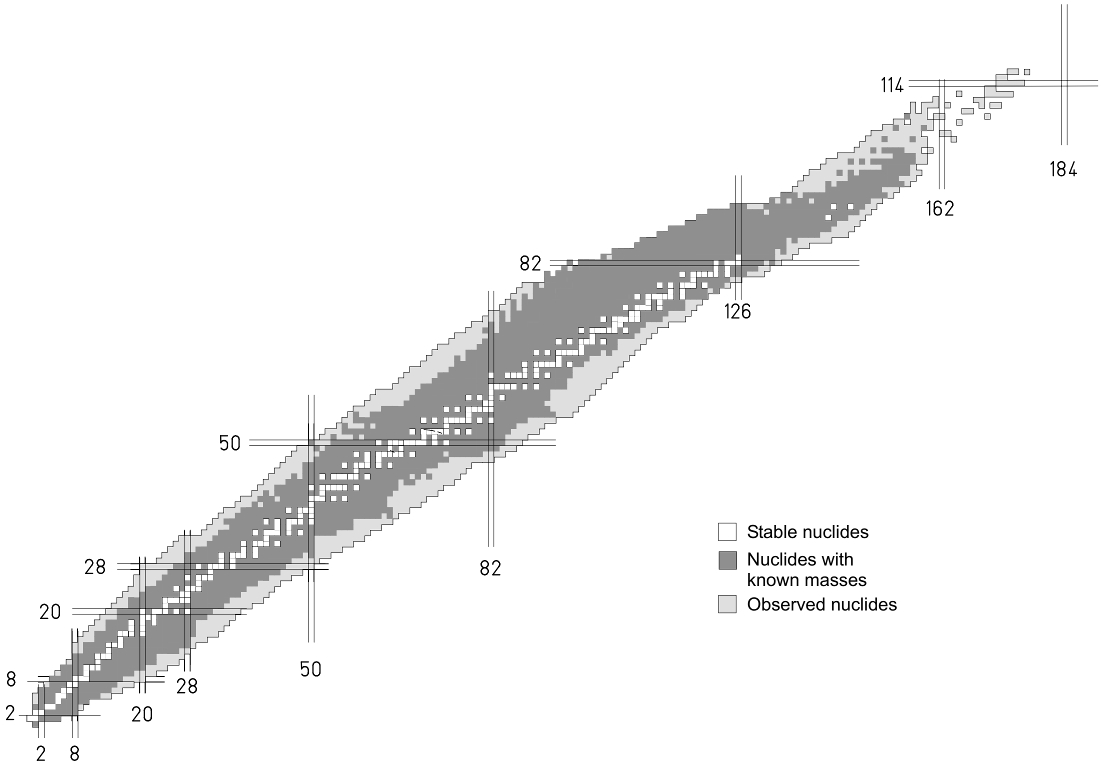

Figure 1.1: The chart of nuclides illustrating the present knowledge of nuclear masses [44].

justments of theoretical nuclear models [2], which are then used to predict nuclear properties of very exotic nuclides, like e.g. superheavy elements or nuclides at the astrophysical r-process path, which extends at least up to the last stable nuclides of thorium and uranium elements. Therefore it is essential for the nuclear theory to obtain new data in this region of the chart of nuclides, in order to test and to improve the available models.

Mass measurements of neutron-rich nuclei in the element range from lead to uranium were pursued in this experiment.

Chapter 2

Experiment

2.1 Experimental setup

2.1.1 Fragment production and in-flight separation with the FRS

The present experiment aimed at the mass measurement of neutron-rich nuclei produced by the projectile fragmentation of an Uranium beam, using the FRS-ESR experimental facilities. At first $^{238}U^{4+}$ ions, produced by the Metal Vapor Vacuum Arc (MEVVA) source, were stripped and preaccelerated to 11.4 MeV/u by the UNiversal Linear Accelerator UNILAC [3], [4]. The resulting $^{238}U^{73+}$ beam, after being further accelerated to energies in the range of 670-690 MeV/u in the heavy-ion synchrotron SIS, hit a 4 g/cm^2 Be target placed at the entrance of the FRagment Separator FRS (see Fig. 2.1). The beam intensities were up to $2{\cdot}10^9$ ions per spill. Various ions with mass numbers smaller than the one of the projectile ^{238}U were then produced by *projectile fragmentation*: according to this

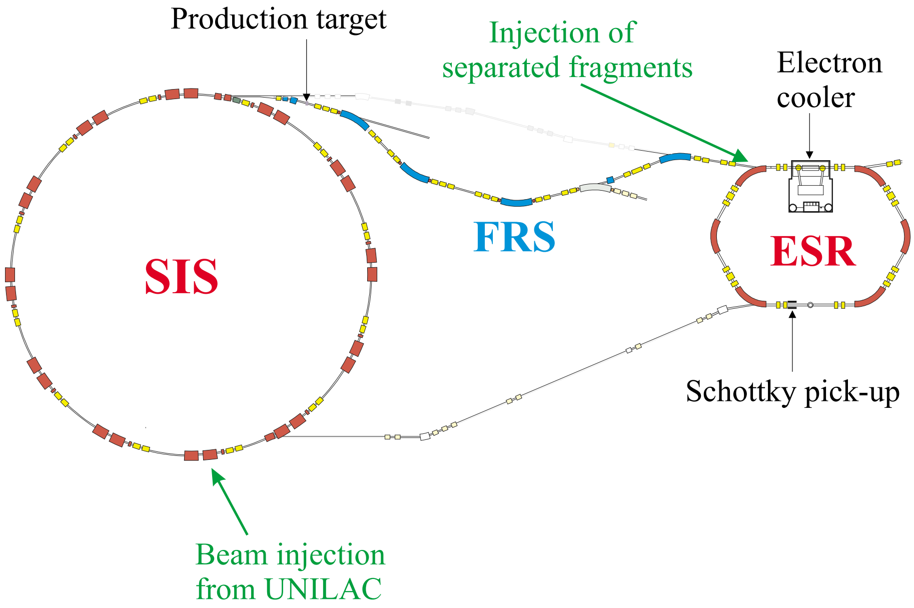
Production target
Injection of separated fragments
Electron cooler
FRS
SIS
ESR
Schottky pick-up
Beam injection from UNILAC

Figure 2.1: The heavy-ion synchrotron SIS, the Fragment Separator FRS and the Experimental Storage Ring ESR, which are used for the present experiment.

mechanism, as the projectile nucleus collides peripherally with the target nucleus, their geometrically overlapping region gets *abraded*, i.e. the overlapping nucleons are removed from the target and the projectile. The remaining "spectator" parts of the target and the projectile (*prefragments*) subsequently deexcite in an evaporation cascade [5]. In addition to projectile fragmentation, charge-exchange and pick-up reactions can also occur with small cross-sections.

The magnetic spectrometer FRS separated the produced ions in-flight according to their magnetic rigidity and focused them on its final focal plane, by using a proper combination of dipole, quadrupole and sextupole magnets [6], [7]. The magnetic rigidity Bρ is expressed as

$$B\rho = \frac{mv\gamma}{q}, \tag{2.1}$$

where m is the rest mass, q is the charge, v is the velocity and γ is the Lorentz factor of the fragments. Only the fragments with Bρ values fitting inside ± 1% of the set magnetic rigidity of the FRS (Bρ_{FRS}) were transmitted through the whole FRS and arrived at its final focus.

The EPAX2 semi-empirical parametrization [8] provided the production cross-sections of the projectile fragments emerging from the target. The atomic energy loss and energy straggling of the incident beam were calculated by the ATIMA programm [9]. The possible charge-state distributions of the produced fragments were predicted by the GLOBAL code [10] which models charge-exchange interactions of relativistic heavy ions penetrating matter. The fragment production and their transmission through the FRS were calculated by the MOCADI [11] and the LISE code [12], which include the aforementioned ATIMA, EPAX2, and GLOBAL codes and take into account the ion-optical properties of the FRS. Fig. 2.2 depicts the expected charge-state abundances of the projectile fragments for an applied experimental setting of a 672 MeV/u ^{238}U^{92+} beam impinging on a 4007 mg/cm^2 Be target with the FRS set at a Bρ= 7.707 Tm, according to a LISE simulation. It is evident that bare nuclei are transmitted in the most neutron-rich area of the studied element range of $80 \leq Z \leq 93$, but that particles closer to the β stability valley are transmitted with several electrons. H-like and He-like ions dominate in the studied energy range and region of the nuclidic chart. Nevertheless, Li-like and even Be-like ions become significant too, especially in the vicinity of the projectile ^{238}U due to their high nuclear production cross-section. The simulated trend of the charge state abundances of neutron-rich fragments contrasts the one in the neutron-deficient area of the nuclidic chart: the charge states of neutron-deficient nuclei increase with increasing distance from stability, while the appearance of Be-like neutron-deficient fragments is highly improbable [21].

2.1.2 Ion injection, storage and cooling in the ESR

The selected fragments exiting the FRS are subsequently injected with energies around 340 MeV/A into the 108.36 m long Experimental Storage Ring ESR which has a Bρ injection acceptance window of ± 0.2% around Bρ_{ESR} = Bρ_{set}. The needed conditions for ESR injection were also implemented by the Monte-Carlo code MOCADI for simulating the present experiment.

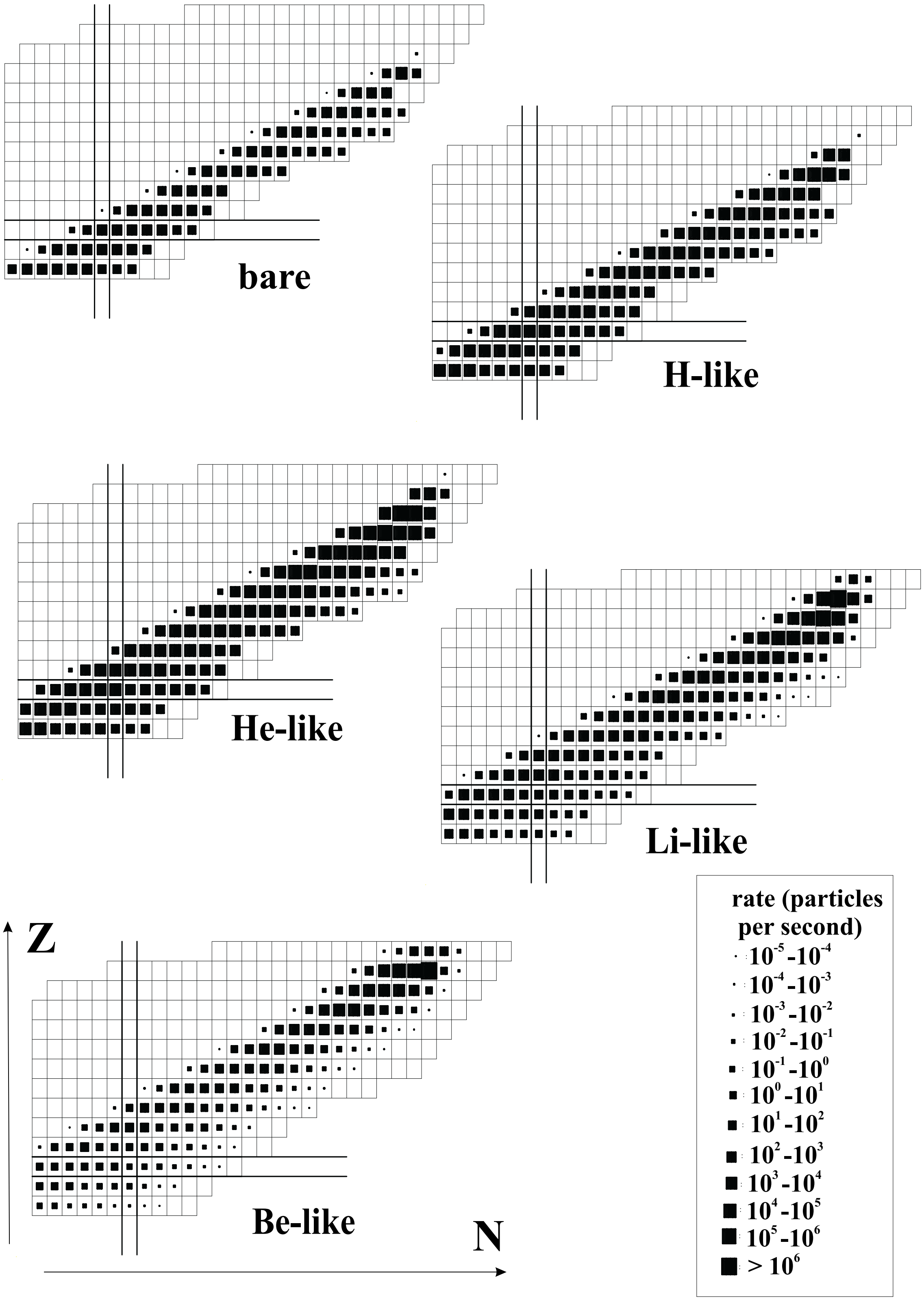

Figure 2.2: Calculated yields of the various possible charge states of fragments produced by a $6.25 \cdot 10^9$ pps intense $^{238}U^{92+}$ beam at 672 MeV/u impinging on a 4007 mg/cm^2 Be target which are transmitted through the FRS, at Bρ= 7.707 Tm and $80 \leq Z \leq 93$.

The injected fragments are stored in the ring and circulate with a revolution frequency f determined by their velocity v and orbit length C

$$f = \frac{v}{C} \tag{2.2}$$

Differentiating (2.1) and (2.2) and combining their results leads to

$$\frac{\Delta f}{f} = -\frac{1}{\gamma_t^2}\frac{\Delta(m/q)}{m/q} + (1 - \frac{\gamma^2}{\gamma_t^2})\frac{\Delta v}{v} \tag{2.3}$$

where

$$\gamma_t^2 = \frac{\Delta(B\rho)}{B\rho}/\frac{\Delta C}{C}. \tag{2.4}$$

The factor γ_t is the *transition point* of the storage ring and depends on its ion-optical properties.

In order to perform accurate mass determinations via revolution frequency measurements one should get rid of the velocity distribution dependence in (2.3). This condition is fulfilled either by tuning the ring to the *isochronous mode* where $\gamma = \gamma_t$ [13], [14], or by minimizing the velocity spread $\Delta v/v$. The latter method is used in Schottky Mass Spectrometry, described in 2.2, by means of an electron cooler.

During every passage through the cooler, which is placed at the first straight section of the ESR (see Fig. 2.1), the ion beam is merged over a length of 2 m with an electron beam. The resulting momentum exchange between electrons and ions attributes after sufficient passages the electron velocity to all the ions as their mean velocity. This velocity is determined by the voltage value applied to the electron cooler electrodes and typically amounts to $0.6 - 0.7$ c, where c is the velocity of light in vacuum. Fig. 2.3 illustrates the FRS transmission, injection into the ESR, storage and electron cooling process for a specific MOCADI-simulated setting of the present experiment with Bρ_{FRS} = Bρ_{ESR} = Bρ_{set}= 7.707 Tm. The various fragments injected in the ring with different velocities are represented by black dots. The ions with velocities $\beta > \beta_{cooler}$ are decelerated to β_{cooler} with a simultaneous decrease of their magnetic rigidity Bρ, according to eq. (2.1), as shown by the dashed arrows pointing downwards. The dashed arrows with upward direction represent the acceleration to β_{cooler} with a simultaneous Bρ increase, of ions injected into the ESR with velocities $\beta < \beta_{cooler}$. Only the ions with a final Bρ value falling inside the storage acceptance of the ESR which is ±1.5% of Bρ_{set} remain in the ring and can be observed (grey dots). It is noted that the ions aimed to be measured appear in the storage ring in various charge states, which offer the great advantage of a redundant mass determination (see section 4.2.2).

The above cooling procedure takes place until an equilibrium is reached between the cooling force and the intra-beam scattering due to Coulomb repulsion. It is completed faster for a higher cooling force F_c, which increases with the ion charge q and the electron density n_e [15]. In Schottky mass measurements one tries to reduce the cooling time by satisfying the above conditions, since it places the lower limit on the lifetime of possibly observed nuclei by this technique. In our case, with an electron density n_e of the order of $10^6/cm^3$ and ions charges q in the range of 85-92, the cooling time varies slightly according to the stored ion species from about 10 s to 20 s.

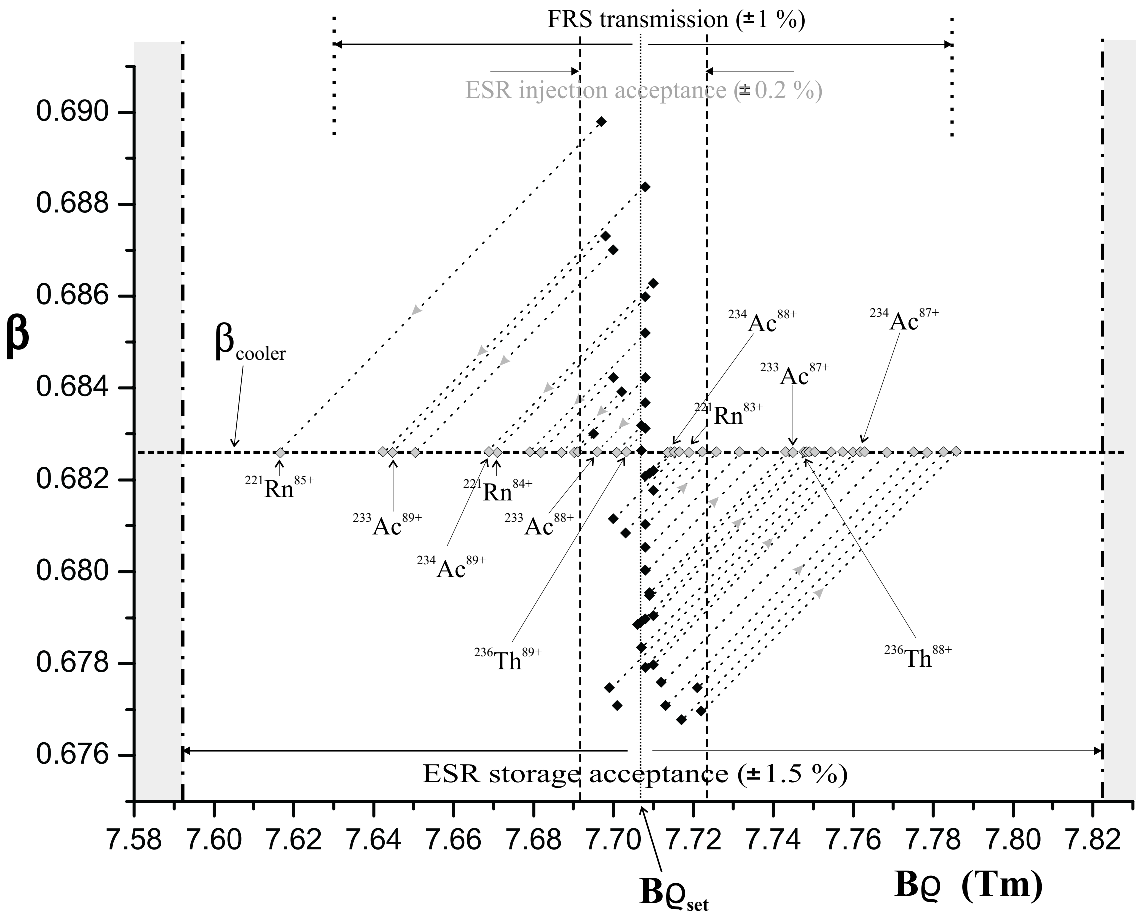

Figure 2.3: Transmission, acceptance and cooling of projectile fragments schematically illustrated in the magnetic rigidity-velocity space. The FRS transmission, ESR injection acceptance and ESR storage acceptance are marked by dotted, dashed and dash-dotted lines, respectively. The dashed arrows represent the cooling of ions injected in the ESR with different velocities $\beta = v/c$ (black dots) and magnetic rigidities inside ± 0.2% of Bρ_{set}=7.707 Tm to the same velocity β_{cooler}=0.6827 (gray dots), by a simultaneous change of their magnetic rigidity. Some triplets and doublets of ions with previously unknown masses that are stored in the ring are selectively indicated.

Electron cooling narrows the initial velocity distribution of $\Delta v/v \simeq 10^{-3}$ to a final value depending strongly on the number of stored particles N_i. Its optimum performance of reducing the velocity distribution by 4 orders of magnitude to $\Delta v/v \simeq 10^{-7}$ is achieved for $N_i \leq 4 \cdot 10^3$ [16]. Such a velocity spread can be considered negligible, making the relative frequency difference $\Delta f/f$ in 2.3 dependent only on the m/q term at a first order approximation:

$$\frac{\Delta f}{f} = -\alpha_p \cdot \frac{\Delta(m/q)}{m/q} \tag{2.5}$$

where α_p is the *momentum compaction factor*, defined as

$$\alpha_p = \frac{1}{\sqrt{\gamma_t}} = \frac{\Delta C/C}{\Delta(B\rho)/B\rho}. \tag{2.6}$$

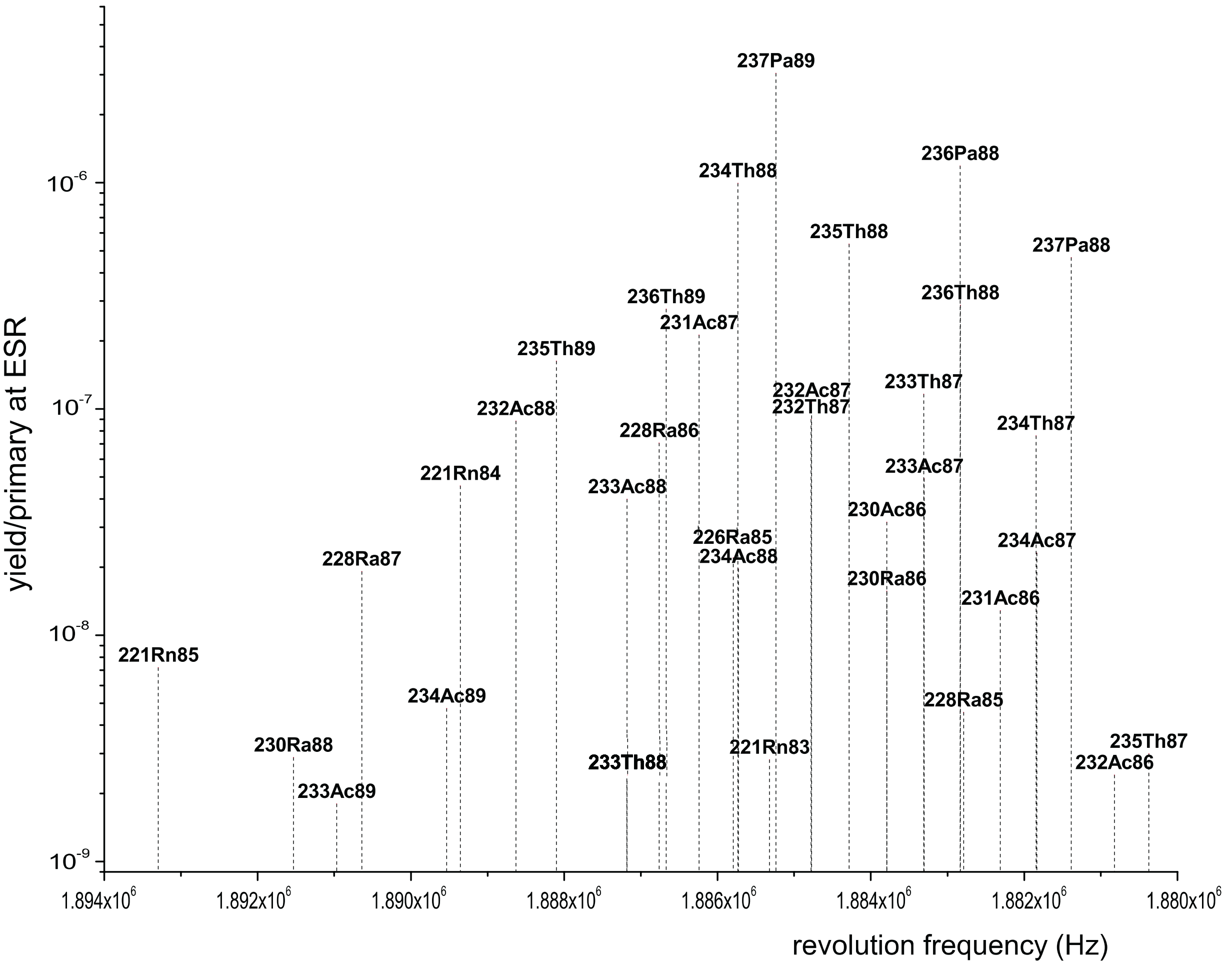

Figure 2.4: Simulated Schottky spectrum for Bρ_{set}=7.707 Tm in terms of revolution frequency in the ESR. The expected peak intensity is represented by the yield per primary beam of the corresponding fragment in the ESR, as calculated by MOCADI.

Another process that can be widely used in future ESR experiments, precooling hot fragment beams thus reducing effectively their phase-space density prior to electron cooling, is stochastic cooling. This technique is based on sampling a particle's motion in the ring with a pickup electrode and correcting this motion with a kicker [17]. It was tested for the first time with fragment beams in the present experiment yielding a total cooling duration of about 5-7 s. About 3 s of stochastic cooling are expected to reduce the time needed for electron cooling to the order of a second [18]. Stochastic cooling was successfully applied in the following Schottky experiment on ^{208}Pb projectile fragments. 6 s of stochastic precooling reduced then the time needed for electron cooling to 2 s [19].

2.2 Schottky mass spectrometry

Schottky mass spectrometry (SMS) is based on Schottky noise spectroscopy which relies on recording and analyzing the revolution frequency of ions circulating in a storage ring or circular accelerator [20]. Two different frequency peaks f_i and f_j in the frequency spectra of the noise power density produced by this method correspond to two different cooled ions with mass-to-charge ratio $(m/q)_i$ and $(m/q)_j$, respectively, and are correlated by eq. 2.5 as follows:

$$\frac{f_i - f_j}{f_i} = -\alpha_p \frac{(m/q)_i - (m/q)_j}{(m/q)_i} \quad ; \quad i, j \ \ integer \tag{2.7}$$

Consequently, unknown masses can be determined via the mass-to-charge ratio of the corresponding ion in relation to ions with known properties present in the same spectrum, provided that the factor α_p is known [21]. This factor's value and shape vary slightly with the ESR magnets settings. Assuming $\alpha_p = 0.1792$, as it was found in the last SMS experiment [22], and considering only fragments with half-lives ≥ 1 s, an expected Schottky spectrum was simulated in Fig. 2.4 for the previously discussed setting of Bρ_{set}=7.707 Tm. The abscissa increases from right to left for accordance purposes with Fig. 2.3.

2.3 Frequency measurements

The ions circulate in the ESR ultra high vacuum system with frequencies $\simeq$ 1.9 MHz, as follows from eq. (2.2) for its mean circumference $C = 108.36$ m and for ion velocities $v = \beta \cdot c$, with $\beta \simeq 0.68$. Every ion revolution produces an image current which is detected via two parallel electrostatic pick-up probes (Schottky pick-ups), see Fig. 2.5. The signal from every electrode is connected to a resonance circuit and preamplified. The sum of the signals is independent of the transverse ion coordinates, containing information only about the ion's longitudinal motion in the ring. Therefore it is further treated, by being amplified and split in two parts. The first one feeds a real time spectrum analyzer for on-line monitoring of the beam, which was employed for the first time in an ESR experiment. This analyzer performs a 1024-point complex Fast Fourier

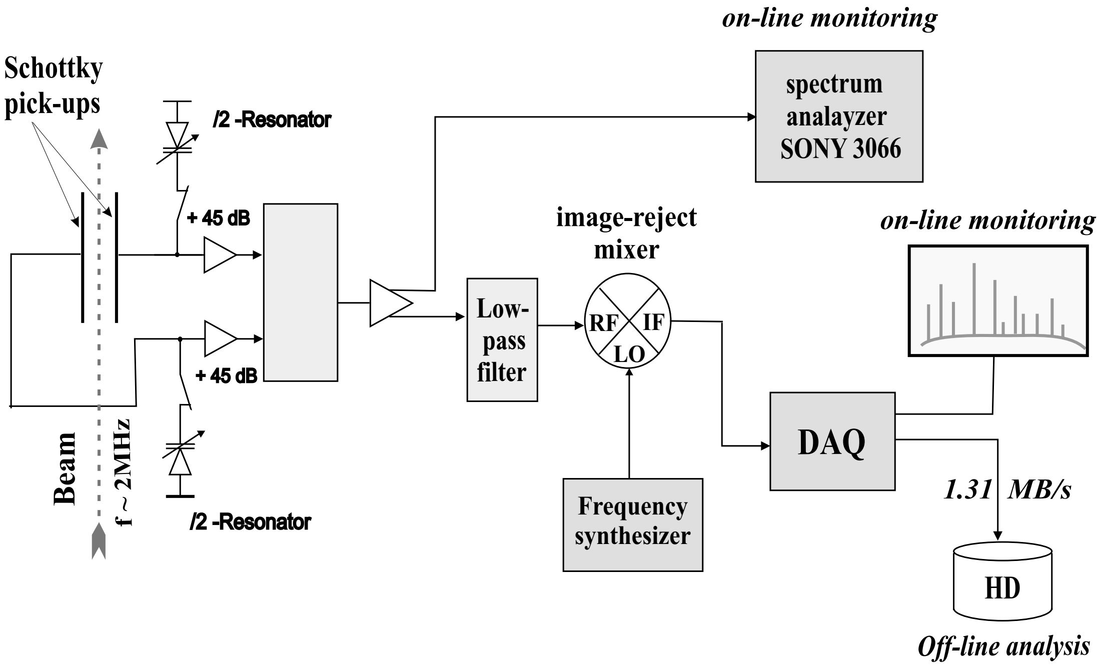
on-line monitoring
Schottky pick-ups
/2 -Resonator
spectrum analayzer SONY 3066
+ 45 dB
image-reject mixer
on-line monitoring
Low-pass filter
RF
IF
LO
+ 45 dB
DAQ
Beam
f ~ 2MHz
/2 -Resonator
Frequency synthesizer
1.31 MB/s
HD
Off-line analysis

Figure 2.5: Experimental setup for Schottky diagnostics at the ESR

Transformation with Blackman-Harris window at 12500 times/s to its acquired signal, after down-converting it. It stores and displays up to 4000 time-subsequent spectra, allowing the observation of dynamic processes of the beam such as its cooling [23].

The second part of the Schottky noise power signal passes through a low-pass filter in order to suppress undesirable higher frequencies. We decided to record the 31st harmonic (h) of the Schottky signal, since the Schottky noise is inversely proportional to frequency and the signal's frequency resolution increases with increasing harmonics as long as they don't overlap [24]. For typical ion revolution frequencies $f_{rev} \simeq 1.9$ MHz, the resulting $f_{rev} \cdot h \simeq 58.9$ MHz frequencies should be sampled with $2 \cdot 58.9 = 117.8$ MHz, according to the sampling theorem [25]. Therefore, in order to sample this signal, it was down-converted to a range of frequencies $\simeq$ 0-300 kHz, by being mixed with a Local Oscillator frequency $LO \approx$ 58.9 MHz, supplied by a frequency synthesizer, in an image-reject mixer [26], [27]. Hence the revolution frequency (f_{rev}) of an ion in the storage ring is related to the frequency (f) supplied by the mixer via the equation:

$$h \cdot f_{rev} = LO + f \tag{2.8}$$

The mixer's output is treated by a newly applied data acquisition system (DAQ) for storing the data for off-line analysis as well as regularly monitoring samples of them on-line.

Chapter 3

Data acquisition system

The main task of this study was to develop and apply a novel system for acquiring the raw data of Schottky experiments, aimed at the following improvements:

- segmenting the data flow from the ADC without interrupting or affecting it, providing flags indicating
  - the actual time
  - the actual experimental conditions

  under which every segment was recorded. Such a segmentation
  - grants immediate access to any desired moment or area of the recorded data with specific parameters
  - allows for location and exclusion of any possibly corrupted data segment while keeping the unaffected segments
- inspecting on-line different stages of the data acquisition:
  - monitoring samples of a running recording
  - monitoring data from a recording already copied to a filesystem

These goals were reached by combining during recording the treated Schottky-noise signal and information from the parameter holding units in a thruput controller. The data acquisition system, based on a VXI crate, is controlled by a usual linux computer by applying a suitable software package. In detail :
The Schottky-noise signal coming from the mixer serves as analog input to the antialising ADC of a VXI crate, as shown in Fig. 3.1. This crate is controlled by the VXI-MXI which is connected to an independent linux computer via a PCI adapter. When the user starts a measurement from the computer, a TTL signal triggers the ADC and the Datum Time and Frequency Processor (TFP) simultaneously [28]. Data collection is then initiated and continues until the ADC would indicate that its internal FIFO memory is overflowed. The ADC is clocked from the TFP which acts as a high precision clock with a 10 MHz sampling frequency, additionally to its own 10 MHz crystal oscillator.
The function of the ADC and SCSI modules is presented in Fig. 3.2: the sample ADC data, after being amplified, are treated by an anti-alias filter that rejects signals above 6 MHz to reduce aliasing. The following precision ADC generates 23 bit outputs at a sample rate up to 10.24 MHz [29]. At the subsequent zooming

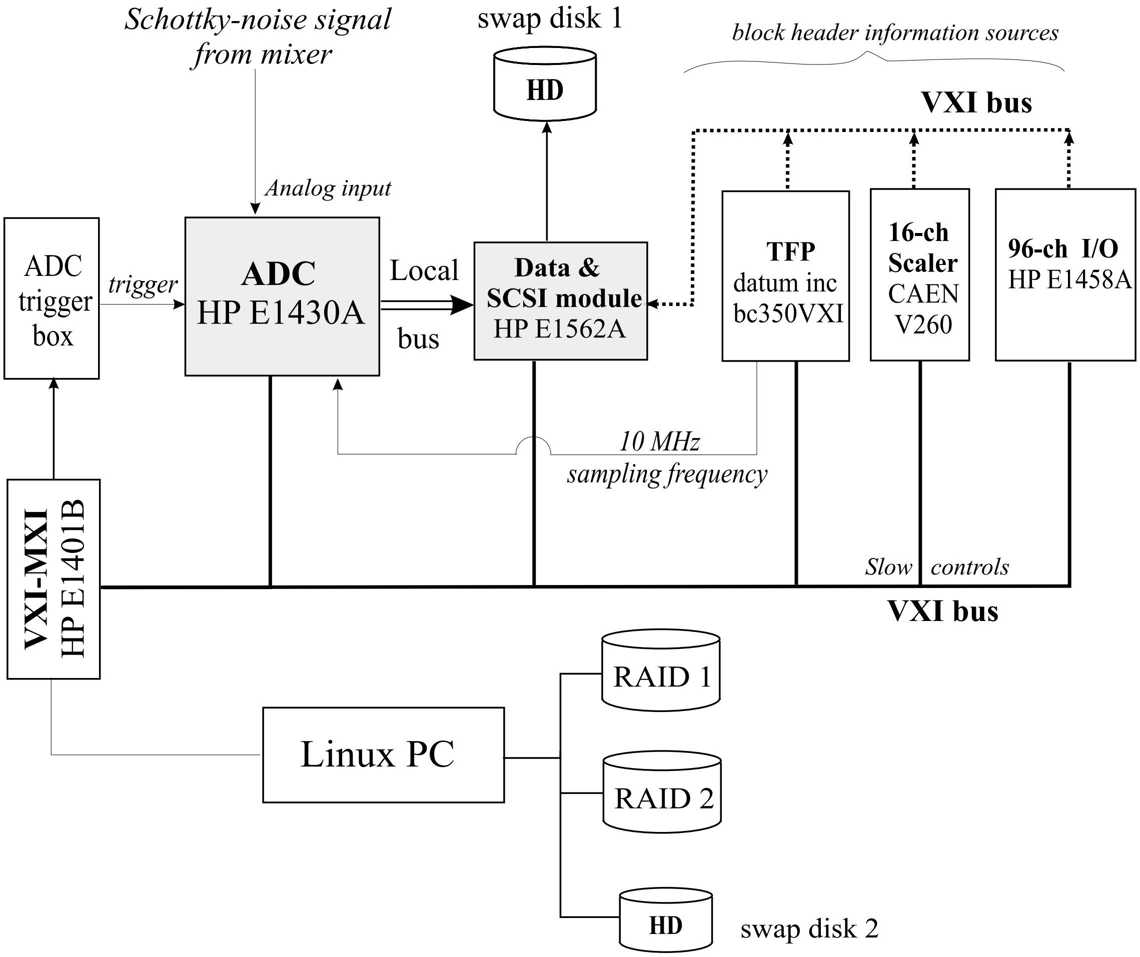
Schottky-noise signal from mixer
swap disk 1
HD
block header information sources
VXI bus
Analog input
ADC trigger box
trigger
ADC HP E1430A
Local bus
Data & SCSI module HP E1562A
TFP datum inc bc350VXI
16-ch Scaler CAEN V260
96-ch I/O HP E1458A
10 MHz sampling frequency
VXI-MXI HP E1401B
Slow controls
VXI bus
RAID 1
Linux PC
RAID 2
HD
swap disk 2

Figure 3.1: Schematic overview of the data acquisition system.

stage a mixer, set to a 160 kHz value, shifts the center frequency of the signal to 0 thereby making it complex. Each of the following digital low-pass filters reduces the bandwidth by a factor of 2. Since the selected decimation level was 5 during the recording, the physical sampling rate of 10 MHz was reduced at this stage to an effective sampling rate of $10^7/2^5 = 312500$ Hz. This represents the final spectral bandwidth, as explained in 4.1.2. The above parameter selections are user-defined in the software that initiates the data recording [28].

The resulting output contains 64 bits, of which 32 represent the real and 32 the imaginary part of the signal. During the data formatting operation we took advantage of the possibility to reduce the precision of every signal component from 32 to 16 bits. The selected complex data of 32 bits = 4 bytes each are stored in the FIFO memory. The separation of the data to segments (blocks) is accomplished by setting flags indicating the separation byte before the recording initialization [28]. We defined it as 32768, setting a flag every $32768 \cdot 4 = 131072 = 2^{17}$ bytes. This number consequently represents the length of a data block. We chose to record 100 such blocks every 10 s, resulting to an individual block duration of 0.1 s. The recording was nevertheless continuous, without any dead time, at a rate of 100 blocks $\cdot\ 2^{17}$ B / 10 s = 1.31 MB/s.

The data can be extracted either by means of a slow VXI bus via a 16-bit register (maximum data flow 2 MB/s) and be read by a controller, or by means of a fast local bus (up to 40 MB/s). We took advantage of the local bus connection,

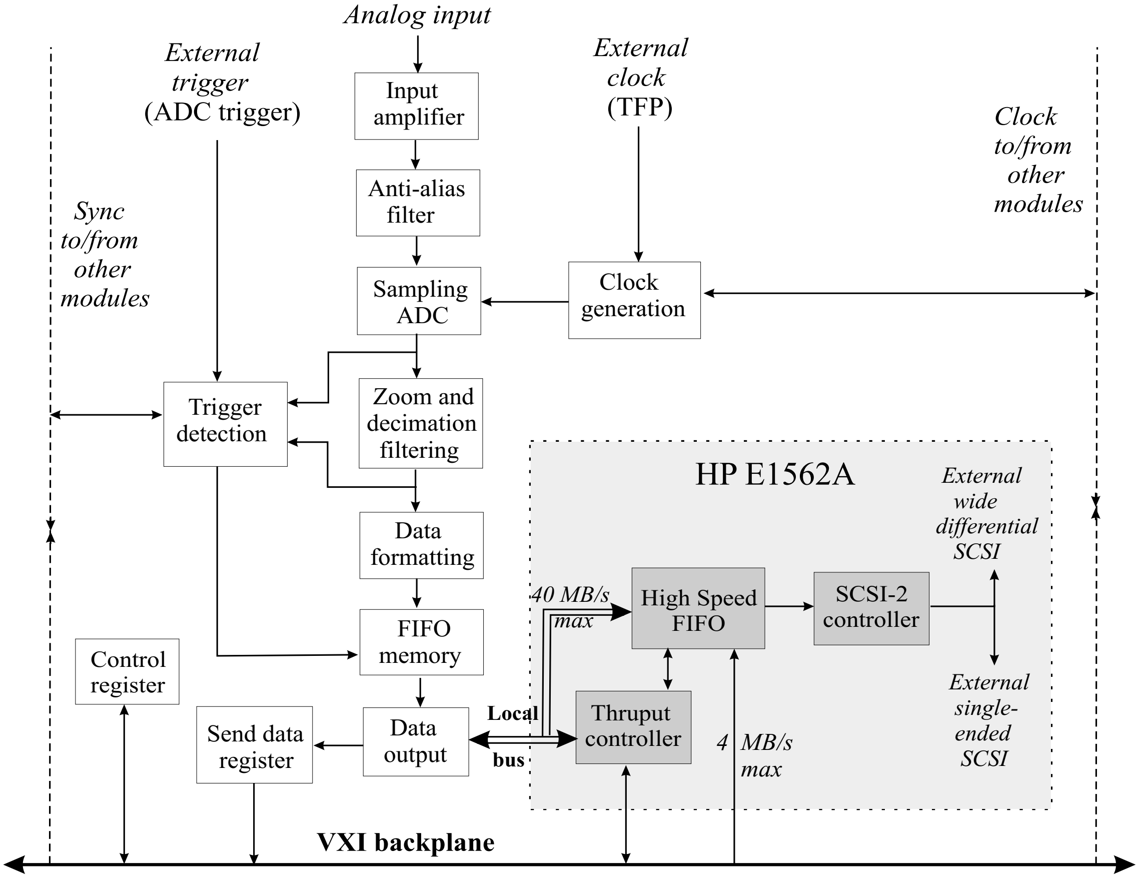
Analog input
External trigger (ADC trigger)
External clock (TFP)
Clock to/from other modules
Sync to/from other modules
Input amplifier
Anti-alias filter
Sampling ADC
Clock generation
Trigger detection
Zoom and decimation filtering
Data formatting
FIFO memory
Control register
Send data register
Data output
Local bus
HP E1562A
External wide differential SCSI
40 MB/s max
High Speed FIFO
SCSI-2 controller
Thruput controller
4 MB/s max
External single-ended SCSI
VXI backplane

Figure 3.2: Block diagram of the ADC module HP E1430A and of the data & SCSI module HP E1562A (gray region).

rapidly transferring the ADC data to the thruput controller and FIFO memory of the adjacent data & SCSI module HP E1562A (see Fig. 3.2). Additionally, the thruput controller receives information about the experimental conditions, transferred via the VXI backplane from the parameter holding modules pictured in Fig. 3.1:

- Timestamps of 0.1 μs resolution in IRIG II standard, which encodes day of year, hour, minute and second data, are read from the TFP unit at the beginning of every data block.
- The values of the cooler voltage and current are collected every 12 s alternatively by a 4 × 24 bits I/O pattern unit.
- The values of the Local Oscillator and those of the control clocks, as well as every new injection, are registered by specific channels of the 16-channel scaler unit.

The SCSI FIFO interleaves the data stream acquired from the local bus with the register values of the devices read from the VXI bus at every data block flag. The data frames containing ADC samples and register values as their headers are subsequently transferred to a SCSI-2 controller and finally written to an external hard disk. The disk has no standard filesystem, in order to speed up the data writing, and in our case it had a capacity of 80 GB. When it is full (after about 16 hours of continuous recording) it is exchanged with an empty one and

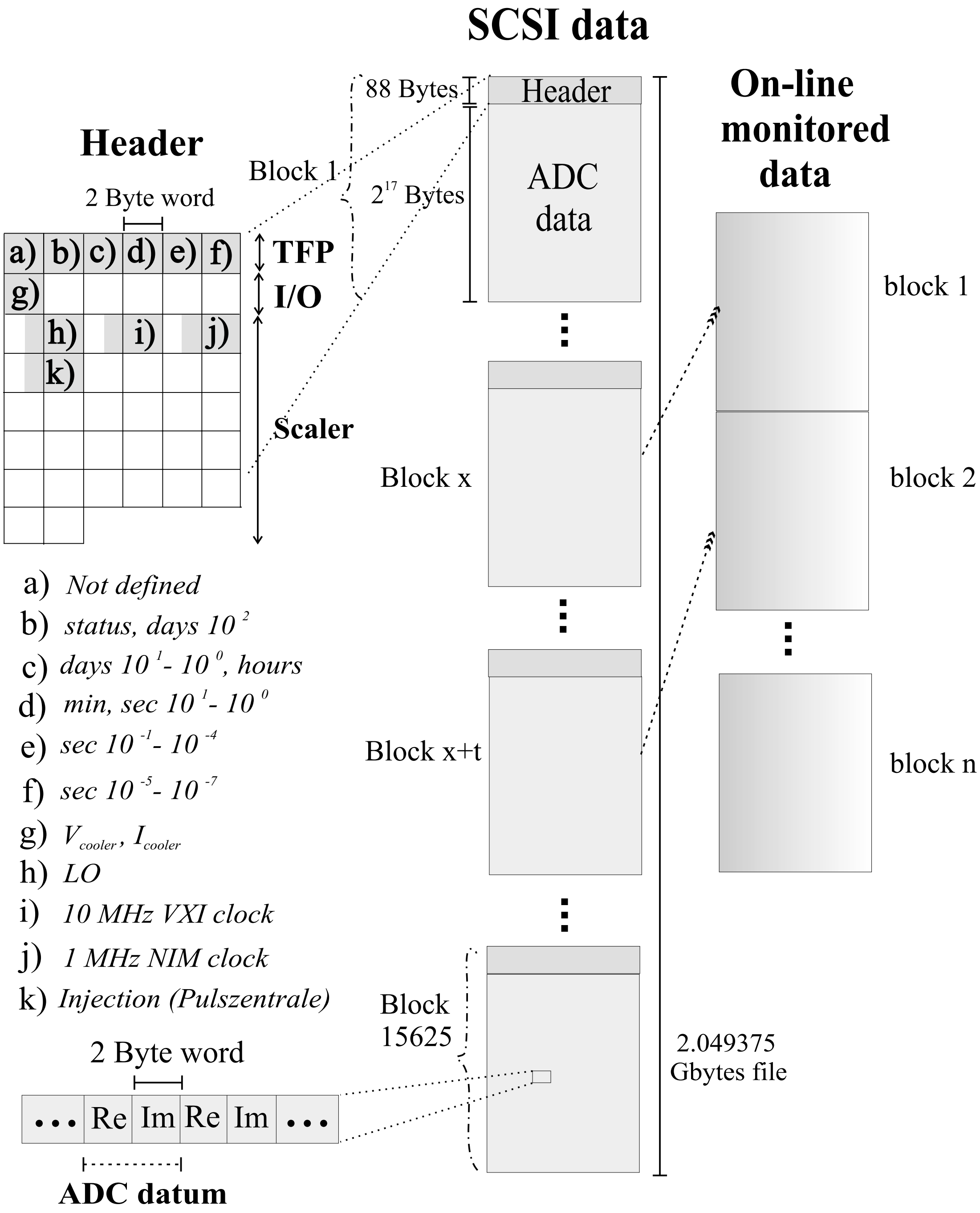
SCSI data
Header
2 Byte word
a) b) c) d) e) f)
g)
h) i) j)
k)
TFP
I/O
Scaler
Block 1
88 Bytes
2^{17} Bytes
Header
ADC data
Block x
Block x+t
Block 15625
2.049375 Gbytes file
On-line monitored data
block 1
block 2
block n
a) Not defined
b) status, days 10^2
c) days 10^1 - 10^0, hours
d) min, sec 10^1 - 10^0
e) sec 10^{-1} - 10^{-4}
f) sec 10^{-5} - 10^{-7}
g) V_{cooler}, I_{cooler}
h) LO
i) 10 MHz VXI clock
j) 1 MHz NIM clock
k) Injection (Pulszentrale)
2 Byte word
... Re Im Re Im ...
ADC datum

Figure 3.3: Format of a file of the SCSI disk data, as stored in the RAID systems (center). Format of the ADC data and of their block headers (left). The grey boxes in the header indicate that the corresponding word holds register parameters, described below. The information from each of the scaler channels occupies 3 Bytes. Sketch of the data extraction for on-line monitoring (right). The numbers x, t and n are integers, t was set to 10.

connected to the linux PC for copying the data to one of the two Redundant Array of Independent Disks (RAID) systems for safe storage (see Fig. 3.1). In order to facilitate their software handling, the final data are split to 2 GB files of 15625 blocks each by the appropriate software [28], when being copied to the linux filesystem. The format of such a file as well as the format of the header, containing information about the recording parameters collected via the VXI bus, and that of the ADC data of every block is described in [28] and depicted in Fig. 3.3. The first 6 words of the header hold time information, the 6 next contain values from the I/O unit and the rest hold the scaler values. How many and which of the words reserved for the I/O and the scaler hold information depends on the applied channel connections and can be varied in each experiment according to the user's needs.

Inspecting the data acquisition procedure on-line is achieved in two ways. The first relies on the regular extraction during recording of one data block from the SCSI disk via the VXI bus and copying it to a file on the controlling linux PC in a simplified format (without a header and with its bytes swaped, see Fig. 3.3). Before recording we defined that every 10th block should be extracted as a monitor sample, meaning that we monitored the data every 10 blocks $\cdot$ 0.1 s = 1 s. Executing the dedicated software one can extract, FFT and average a requested amount of data frames, obtaining a noise power spectrum with 2^{15} frequency channels that corresponds to the selected portion (10 % in our case) of the data which are subsequently written on the external hard disk [28]. The data currently copied to the PC after splitting are also inspected by extracting, FF transforming and averaging selected blocks of the 2 GB data files, providing a noise power spectrum with 2^{15} channels [28].

In total, 4 series of measurements have been recorded, the first one holding 9 and each of the other three 36 2GB data files. Every series contains an automatically created text file containing information about the ADC parameters during the recording. The available series were copied for safe storage to the RAID2 system, which was later found to have randomly corrupted ≈ 0.8 % of the data stored in it, due to the fact that 2 of its disks had some broken segments. The FFT of these corrupted raw data produced a 2 orders of magnitude higher background than that of unaffected files, indicating a very strong impact of possible raw data errors on the spectral background level. This fact also points out the importance of segmenting the data flow, allowing the location and exclusion of corrupted areas of the raw data. All the broken series were managed to be repaired except for the second one.

Chapter 4

Data analysis

4.1 Data handling

4.1.1 Raw data information extraction

In order to transform the raw data contained in the RAID disks to Schottky noise power spectra over frequency for a selected time span, one needs to read the header information of every block and to apply a Fast Fourier Transform to its main part after swaping its bytes. The developed software retrieves from the header the timestamps and the I/O and scaler values as suggested in [30] and in [31] and [32], respectively. Since the scaler channel holding the LO values was found to malfunction during this experiment, these values were retrieved from the logbook. In the following experiment [19] the reading of the LO was successfully achieved by registering it via the I/O pattern unit.

4.1.2 Creation of Schottky noise spectra

The main body of a data block contains 2^{17} Bytes corresponding to $N = 2^{15}$ $= 32768$ complex numbers, each consisting of a 2 Byte word representing the amplitude and a 2 Byte word representing the phase of the Schottky noise signal in the time domain (see Fig. 3.3). Performing a discrete Fourier Transform, the N time points h_k are converted into an equal amount of frequency points H_n, according to

$$H_n = \sum_{k=0}^{N-1} h_k \cdot e^{2\pi i k n/N} = \frac{dP}{df}, \tag{4.1}$$

where k and n are integers. The numbers H_n constitute the Schottky noise power density spectrum dP/df.

The needed amount of operations for computing the above transform can be reduced from N^2 to $N log_2 N$ by implementing the Fast Fourier Transform (FFT). The FFT algorithm separates the even- and odd-numbered points of the original N, hence expressing a discrete Fourier transform of length N as the sum of two discrete Fourier transforms, each of length $N/2$ [33], [25]. This *interlaced decomposition* pattern continues until there are N time domain samples of 1 point length each and is carried out by a bit reversal sorting algorithm. The N frequency spectra corresponding to these N time domain signals are calculated and synthesized into a single frequency spectrum.

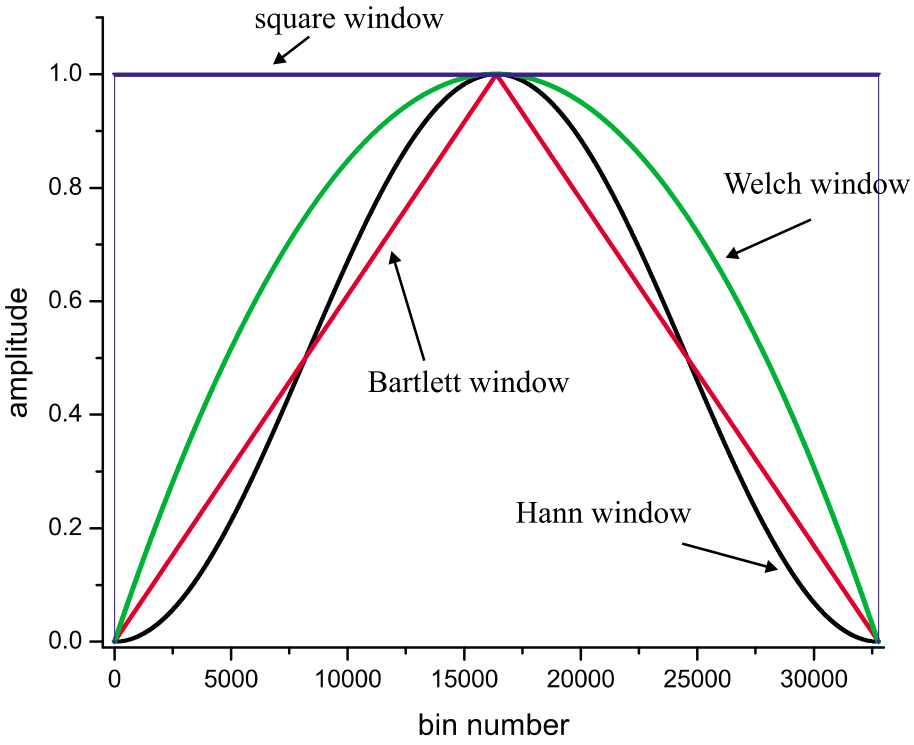

Figure 4.1: Window functions commonly used in FFT power spectral estimation, here plotted over $2^{15} = 32768$ bins.

Performing a FFT of a finite data sample is equivalent to multiplying an infinite data sample by a window function in time, one that is zero except during the total sampling time when it is unity (square window, see Fig. 4.1). The rapid turning on and off of this window function causes "leakage", i.e. the amplitude of the FFTed signal is distributed to its neighboring frequency bins [33]. In order to reduce these sidelobes, one can apply a window function that changes more gradually between zero and unity. Such possible windows are given by eq. 4.2 and plotted in Fig. 4.1 .

$$w_j = \begin{cases} \frac{1}{2}\left[1 - cos(\frac{2\pi j}{N})\right], & Hann \\ 1 - \left|\frac{j-\frac{1}{2}N}{\frac{1}{2}N}\right|, & Bartlett \\ 1 - \left(\frac{j-\frac{1}{2}N}{\frac{1}{2}N}\right)^2, & Welch \end{cases} \tag{4.2}$$

We applied the Hann window which was set as a default for the FFT and was satisfactorily used in previous Schottky mass measurements [22], [24], [27]. Every data segment of length 2^{15} was multiplied (bin by bin) by this window function before the FFT was computed.

The total power P is given by the integrated power density over the Nyquist interval from $-f_N$ to f_N, which is expressed by the mean squared amplitude of the signal:

$$P = \int_{-f_N}^{f_N} \frac{dP}{df} df = \frac{1}{N} \cdot \sum_{j=0}^{N-1} |h_j|^2 \ , \quad j \ integer \tag{4.3}$$

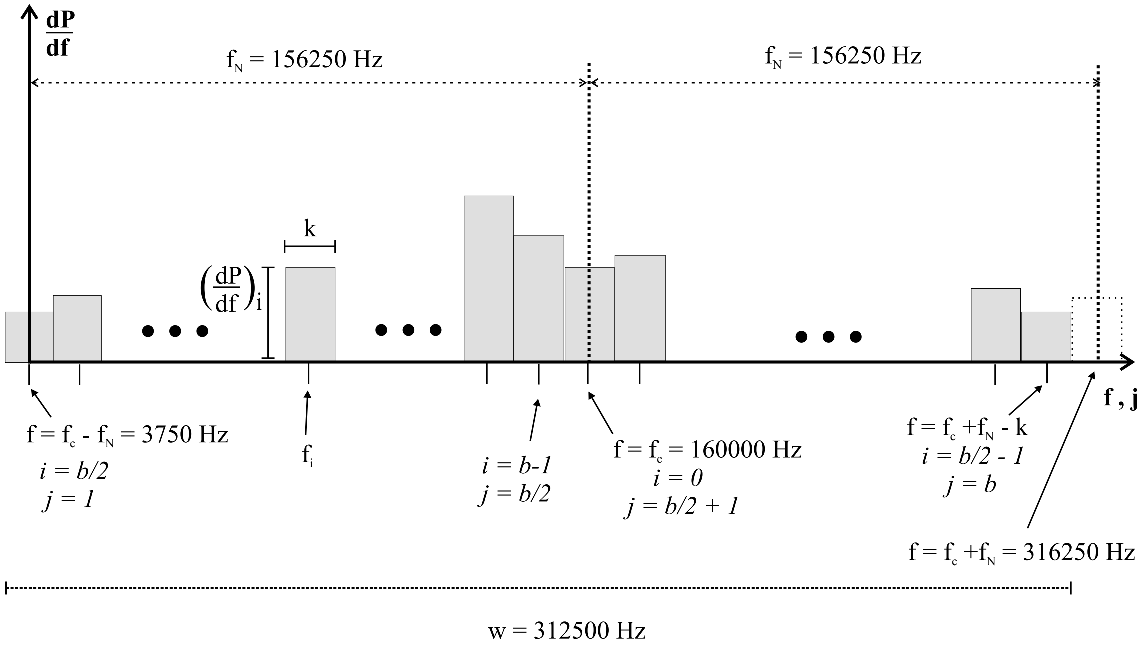

Figure 4.2: Scheme of the x-axis calibration of a Schottky power spectrum. The bin size is increased for display purposes.

The total power over a selected peak region represents the area of this peak and is proportional to the number of particles that form it [24].
The critical Nyquist frequency f_N is defined by the sampling theorem as half of the sampling frequency [25], thus $f_N = 312500/2 = 156250$ in our case. Each value $(dP/df)_i$, $0 \leq i < b$, is assigned to a bin j, $0 \leq j < b$, of center value f_i, $f_c - f_N < f_i < f_c + f_N$. In case the raw data are complex, the frequency f_i of every bin depends on their imaginary part. A check of our data revealed that the phases were distributed around zero with a variation of 10^{-5} at most. We considered the frequency variation due to the phase negligible for the purposes of our experiment and treated only the amplitudes of the raw data, acquiring equidistant channels after the FFT with center frequencies given by eq. 4.4. Nevertheless, there is careful consideration needed in future experiments about keeping or ignoring the imaginary part of the raw data.

$$f_i = \begin{cases} f_c + w \cdot \frac{i}{b}, & 0 \leq i < \frac{b}{2}, \quad \frac{b}{2} + 1 \leq j < b \\ \\ f_c + w \cdot \frac{i-b}{b}, & \frac{b}{2} \leq i < b, \quad 1 \leq j < \frac{b}{2} \end{cases} \tag{4.4}$$

where the size of a block b represents the amount of its points, w is the bandwidth of the spectrum and f_c is its central frequency. The spectrum bandwidth is given by

$$w = f_{max} - f_{min} = (f_c + f_N) - (f_c - f_N) = 2f_N = 312500Hz \tag{4.5}$$

Since the central frequency f_c of 160 kHz is assigned to the bin $j = (b/2) + 1$ and $w = 312.5$ kHz, the first bin ($j = 1$) acquires a central frequency of 3750 Hz and the last one ($j = b$) the closest possible frequency to 316250 Hz, depending on the bin width (see Fig. 4.2). The width k of a bin is defined as

$$k = \frac{w}{b} = \frac{2f_N}{b} \tag{4.6}$$

4.1.3 Optimization of spectral parameters

The created Schottky spectra should reflect the physical phenomena relevant to our study as clear as possible. Therefore, they should correspond to the most suitable time scale and have an enhanced signal-to-noise ratio, a reduced noise spread and the maximum frequency resolution possible. These conditions can be met by properly combining the following methods of data treatment:

- merging a specific amount of subsequent data blocks into one and performing a FFT on the resulting block
- averaging a selected amount of blocks after the FFT.

Fig. 4.3 suggests that averaging some FFTed data blocks increases the baseline B of the spectral background but drastically reduces the background's width. It is obvious that the more the averages N_{av} the narrower the background spread σ_b becomes, since the baseline B is similar in all studied averaged cases. This fact is expressed by the experimentally verified relation [24]

$$\frac{\sigma_b}{B} = \frac{1}{N_{av}} \tag{4.7}$$

Applying a high N_{av} wipes out the random noise fluctuations and jitters due to small fluctuations of the ESR magnetic field, but can smooth down peaks of short-lived ions to the background level. Therefore, a compromise has to be made

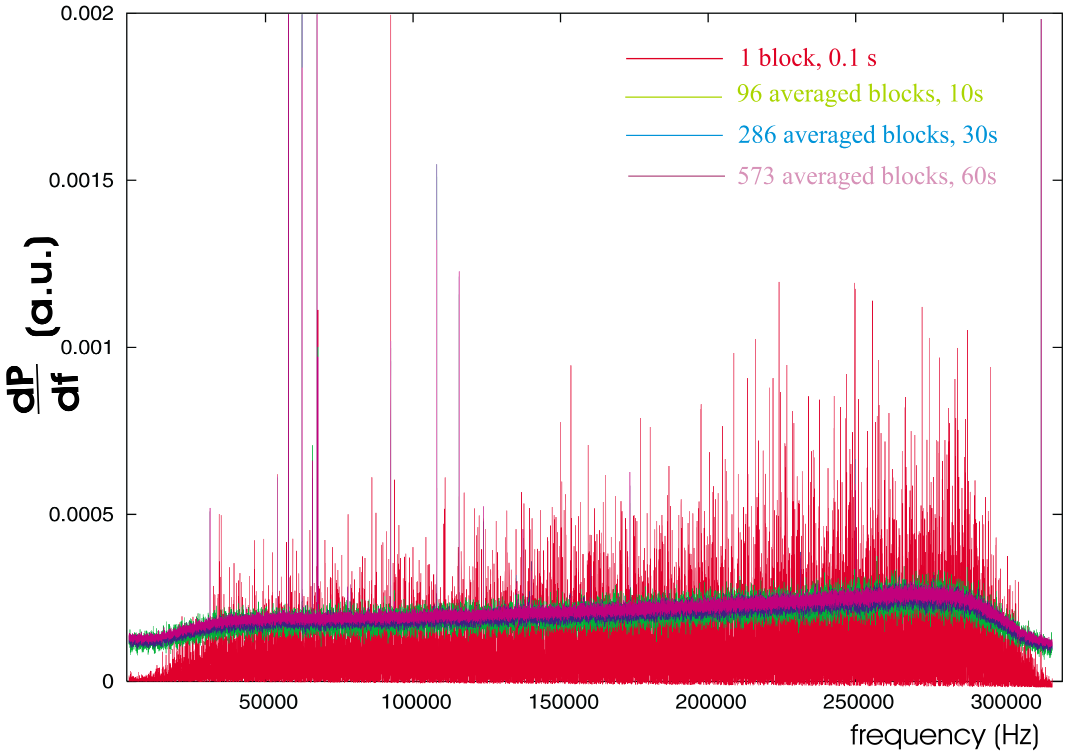

Figure 4.3: Schottky noise power density spectra with a common starting block, produced by averaging over different amounts of blocks, thus corresponding to different time durations. They contain real peaks and spurious peaks due to electronic noise, with a predominant line at 312500 Hz representing the sampling frequency.

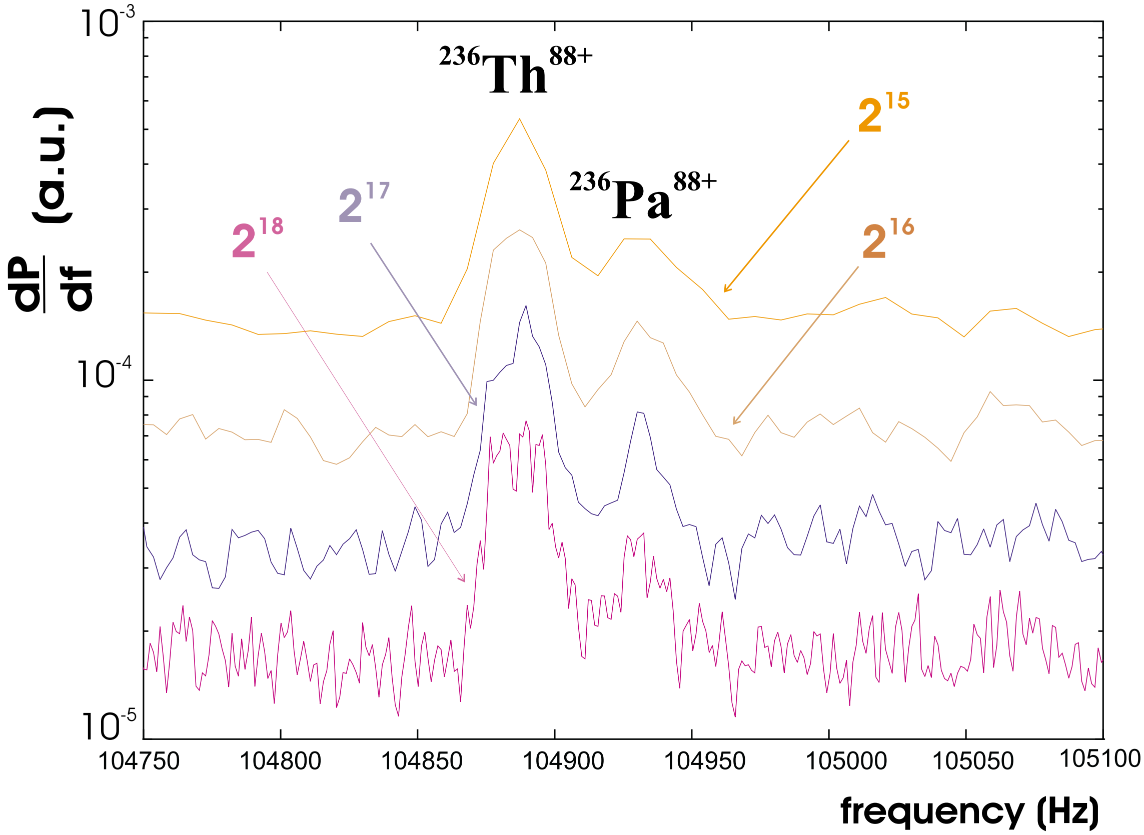

Figure 4.4: 30 s spectra analyzed with a different number of channels, zoomed on an *A=236, Q=88+* doublet.

between detecting real signals out of the noise and observing the time evolution of the represented ions, depending on their lifetime. Averaging over 286 contiguous blocks that correspond to 30 s of continuous measurement serves the purpose of mass determination of the nuclides of interest. Spectra of shorter duration, such as 10 s, are more suitable for half-life studies.

Combining 2^n succeeding data blocks in one by skipping their headers and performing a FFT on the resulting $0.1 \cdot 2^n$ s long block increases the number of frequency bins b with a subsequent decrease of the bin width k according to eq. (4.6), while the total noise power of every peak remains constant. The frequency resolution of the spectra is subsequently modified. A qualitative comparison of the resolution for n = *0, 1, 2, 3* , resulting to spectra with 2^{15}, 2^{16}, 2^{17}, 2^{18} points respectively, is shown in Fig. 4.4 for an *A=236, Q=88+* doublet. It is obvious that at least 2^{16} frequency channels are optimal for clearly resolving two neighboring peaks. A further increase of the number of channels to 2^{17} or more introduces additional structures because of over-binning.

Fig. 4.5 presents a systematic study of the variation of the signal-to-noise ratio with the number of frequency bins for some clearly discernible peaks of a specific Schottky spectrum. Peaks in the 2^{18}-point spectrum couldn't always be satisfactorily fitted, due to their abnormal shape. One can observe that increasing the number of bins deteriorates the peaks' signal-to-noise ratio.

In conclusion, it follows that creating spectra with $2^{16} = 65536$ channels provides the optimum frequency resolution with a satisfactory signal-to-noise ratio. Such spectra were studied in the present work, ranging in frequency from 3750 to

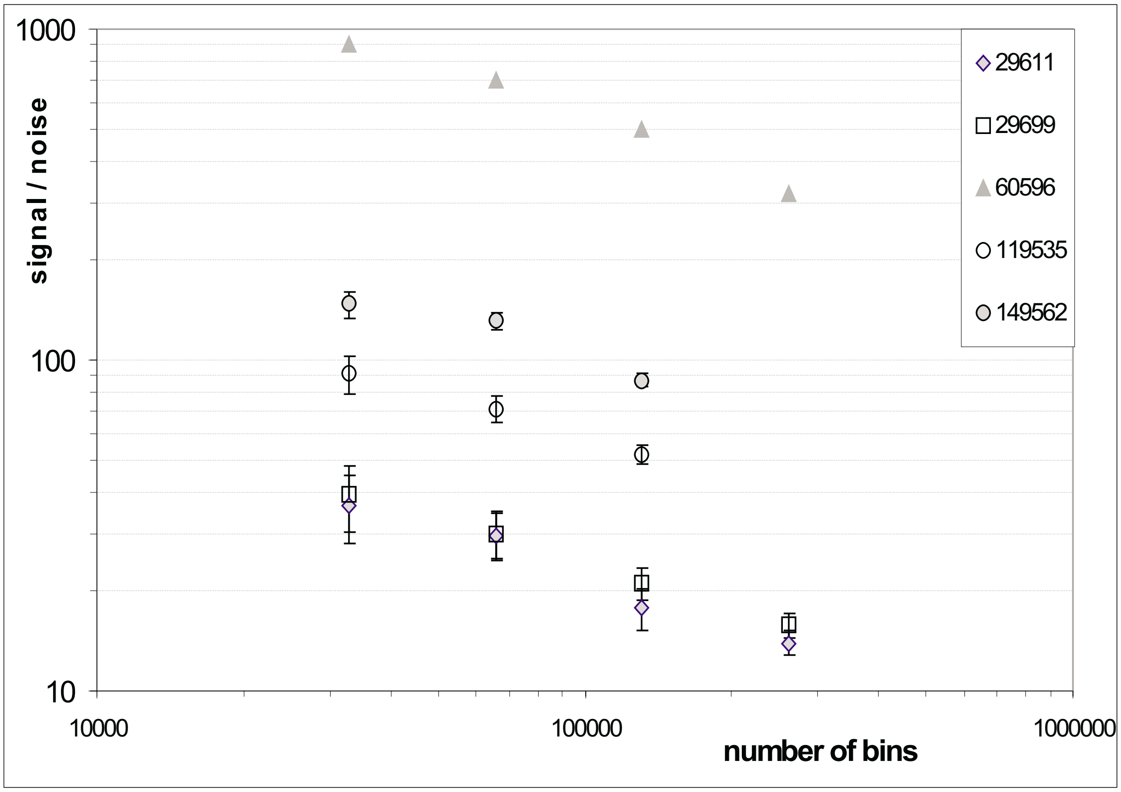

Figure 4.5: Comparison of the signal-to-noise ratio of different peaks of a 30 s Schottky spectrum for various numbers of frequency channels. Noise refers here to the background's width. The displayed peaks are caused by different numbers of particles. Their frequency is given in Hz on the upper right corner. The scale of both axes is logarithmic.

316245.2316 Hz, with a channel width of 4.7683 Hz as resulting from eq. (4.6). Since the Schottky noise is recorded continuously, spectra can be produced at any moment of the recording data flow. In order to study the behavior of an ion bunch in the ring under stable conditions, a group of several contiguous spectra covering the corresponding time interval are created. The first spectrum of such a group starts from the block during which the injection took place or from the block during which the cooler and LO parameters were stabilized. The index of a block during which a change was introduced is provided by reading and comparing the header values of contiguous blocks of a data file according to Fig. 3.3.

4.1.4 Comparison to relevant Schottky experiments

Compared to the previous Schottky mass measurements experiment of 1997, analyzed in [22], the present experiment yielded spectra with a 400 times lower background offset and a 1000 times lower signal-to-offset ratio. One explanation for our weaker signals would be that the ADC was apparently operating to the lower end of its input voltage range. Amplifying the ADC input signal coming from the mixer is expected to increase the noise power density of the acquired Schottky spectra.

The lower signal-to-offset ratio is supposedly caused by the fact that although the applied ADC and mixer-rejector were the same in both experiments, they have functioned in a different way, as suggested by Fig. 4.6: during the 1997 experiment, the ADC was adjusted from -700 to -2100 symmetrically around an offset value of -1400, meaning that its dynamic range was 1400. In the presently analyzed September 2002 experiment the offset of the input amplifier of the ADC was nulled, but a few counts of much higher amplitudes (-8250, +8250) appeared during the time interval of 20 s required to settle the ADC calibration to its specified accuracy [34]. Therefore, the amplification range of the ADC was misadjusted, leading to a low amplification of the main part of the raw data, as indicated by their narrow amplitude distribution in Fig. 4.6 from -170 to +170. After the run it was found out that the mixer-rejector produced noise if a frequency lower than the LO frequency was present. Fixing the mixer led to increasing the ADC dynamics from 340 to 720 in the next experiment of February 2003 [19] (see Fig. 4.6). In all three displayed cases the dynamic range of the ADC was far from optimal, though. The applied security margin was too high, leading to not using all the available bits of the ADC.

Additionally, tuning the mixer during the February 2003 run allowed us to get rid of spurious peaks caused by electronic noise, such as those clearly seen in Fig. 4.3. Fig. 4.7 presents a spectrum recorded without beam on that experiment, averaged

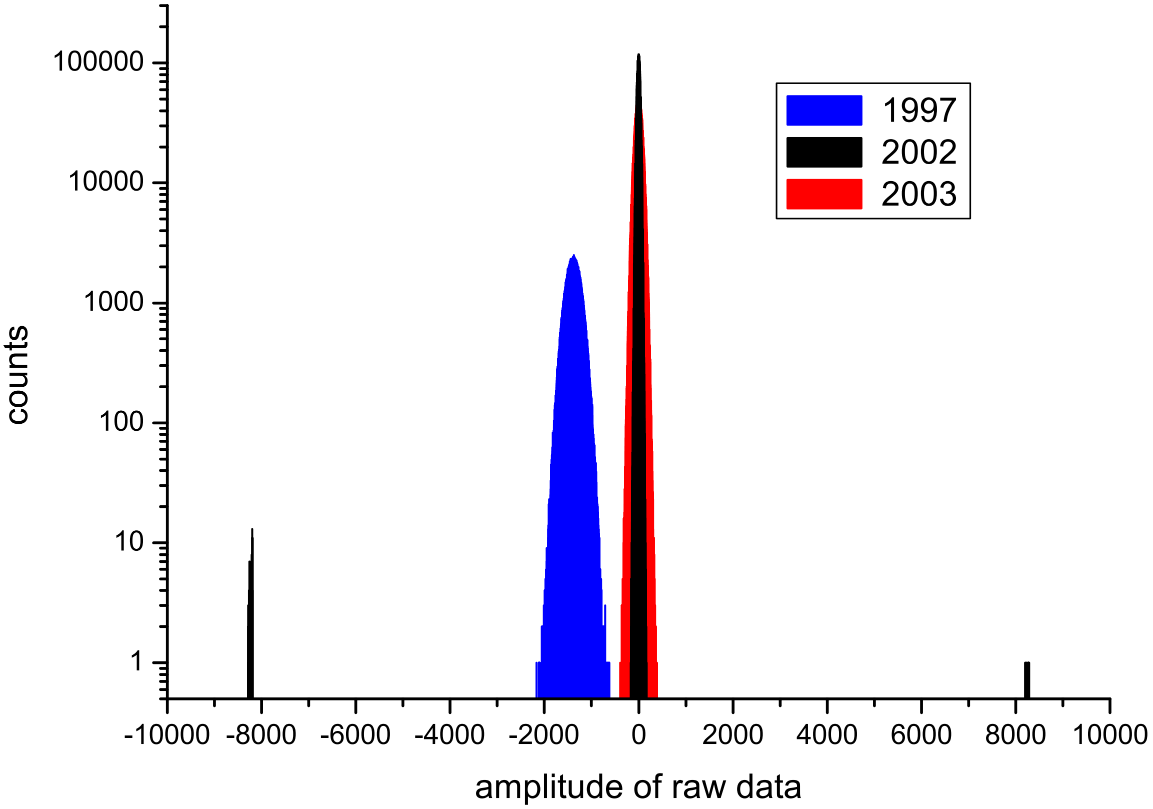

Figure 4.6: Histogram of the real part of the raw data amplitudes taken over a 10 million points sample from the Schottky mass measurements experiments of September 1997, September 2002 and February 2003, respectively. The x-axis of -32768 to +32768 has been zoomed from -10000 to +10000 for display purposes.

over a different number of blocks. A higher number of FFT averages obviously reduces the background width. The only apparent spurious peak represents the DC component of the signal, corresponding to the sampling frequency of 312500 Hz. A feasible improvement for the next Schottky measurements would be to introduce an offset of $\approx$ 1 MHz to the mixer-rejector. Then the DC noise would be avoided, the mixer would not have to reject any negative frequencies and the higher resulting frequencies would be transported with less noise by the coaxial cables [35].

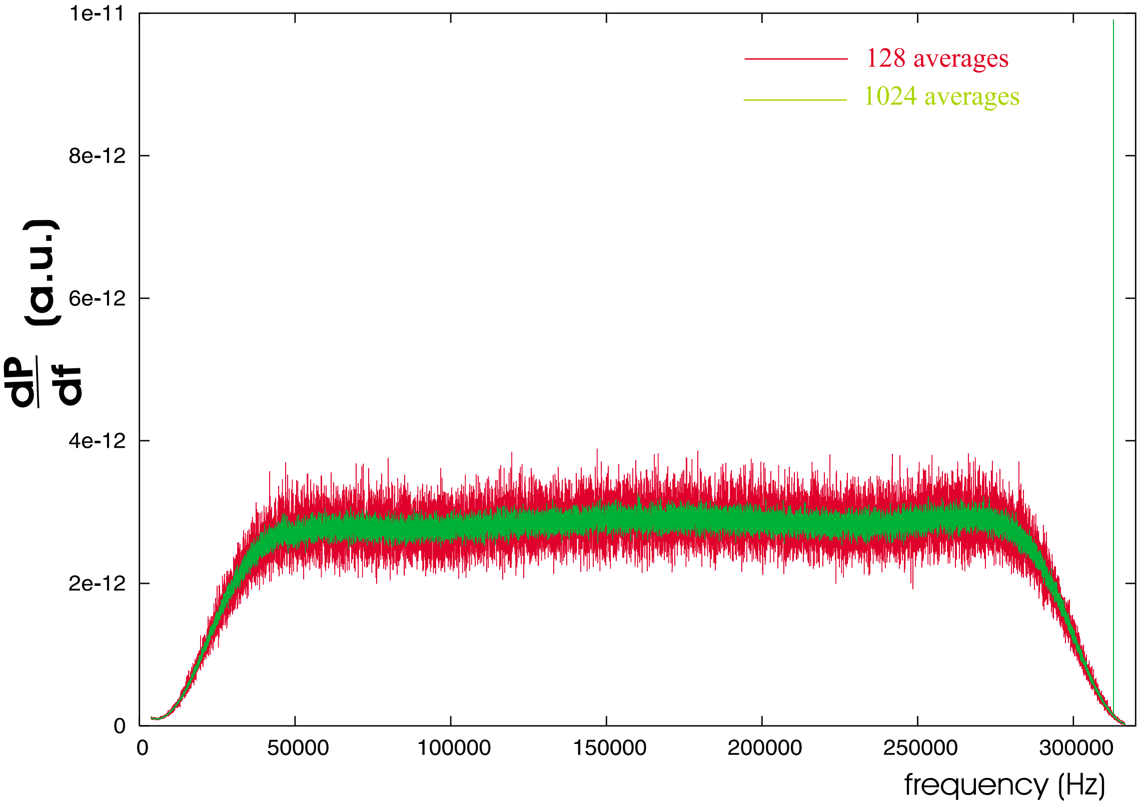

Figure 4.7: A Schottky noise power spectrum recorded without ions in the ESR during the February 2003 Schottky experiment, averaged over 128 and over 1024 blocks.

Since the overflow indicator did not show any overflow during the recording, an additional source of the relatively higher background observed in our experiment may have been a bipolar signal with a frequency too high to be sampled by the ADC. A suggested countermeasure for next experiments would be to sample the mixer signal with one positive and one negative discriminator in order to detect such bipolar signals and to exclude the blocks during which both discriminators count [35].

4.2 Spectrum analysis

The spectra used for our mass analysis have 2^{16} channels each and are averaged over 143 blocks. The background of every spectrum was fitted by a 5th order polynomial in 50 kHz steps and the resulting baseline was subtracted from the spectrum. The remaining random noise fluctuations that constitute the background's width are cut by cutting 2 standard deviations from the Gaussian fit of the projection of the spectrum without the peaks on the Y axis. Afterwards a peak finding routine attributes a peak to risings of the noise power density of at least 3 adjacent channels. A Gaussian fit using the MINUIT package of CERN library is applied to the peaks found. The above peak finding and fitting procedure is very similar to the ones applied in [22], [27] and [36].

The Schottky power spectra can be pictured either in a plot of noise power density over frequency or in a representation where the frequency remains the ordinate axis, time flows in the coordinate axis and the intensity of the peaks is demonstrated by a color code (see Fig. 4.8). Such a waterfall diagram allows the observation of the cooling and decay processes of the stored ions, thus facilitating their identification and enriching our knowledge of their physical properties. Moreover, it makes obvious even slight changes of the LO and cooler parameters, as well as instabilities of the magnet power supplies, by frequency shifts of the same amount and in the same direction of all the real peaks of a spectrum. The spurious peaks, caused by noise from the electronic devices, are unaffected by such changes and therefore easily recognized and excluded from further analysis. The overall frequency drifts can be calculated for all the peaks of every subsequent spectrum and the peak frequencies can be corrected accordingly [22]. Anyhow, for the purpose of mass calculation the drift corrections are not necessary since the peak frequencies are correlated separately in every individual spectrum, in contrast to half-life studies where accurate mean peak frequencies are needed.

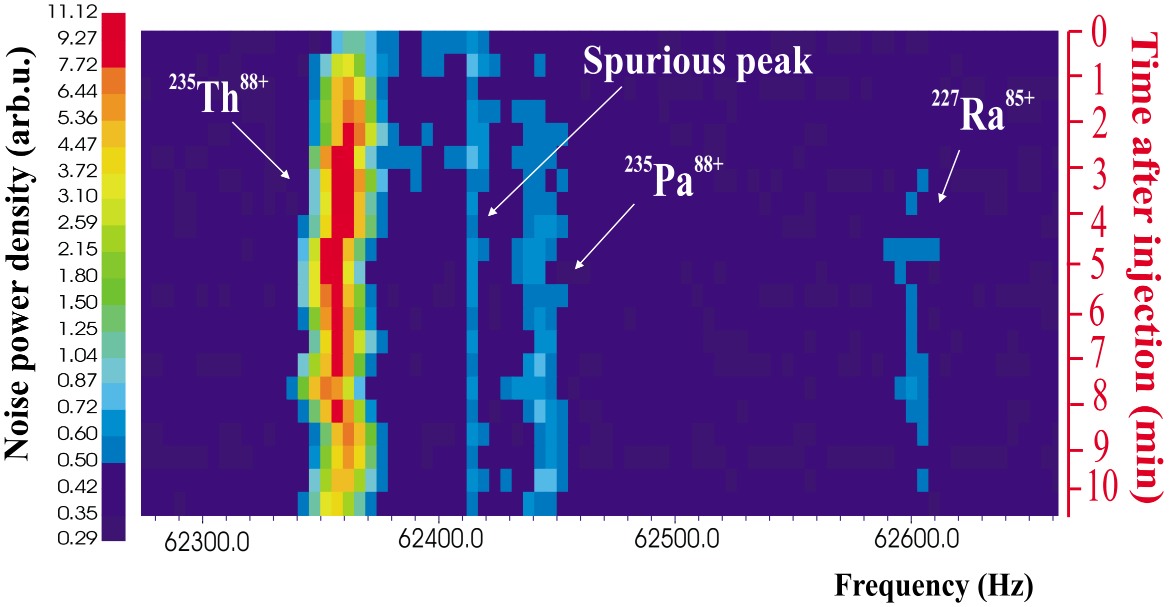

Figure 4.8: A waterfall diagram of a Schottky spectrum zoomed on the A=235, Q=88+ doublet and the $^{227}Ra^{85+}$ peak, that exhibit frequency jitters in the same direction. A spurious peak caused by electronic change has a stable frequency.

Fig. 4.9 shows a mixture of ^{236}Pa^{88+} ions and ^{236}Th^{88+} ions whose mass was determined in this study for the first time, which becomes resolved $\simeq$ 15 min after injection. This observation can be explained by the theory developed in [37] and [38]: the two different ion species circulate with the same velocity on very close orbits in the ESR. At the beginning of the injection, both ion clouds are composed of so many particles that the clouds overlap; thus, both ion species

are locked into the same frequency. About 15 min later, the $^{236}\mathrm{Pa}^{88+}$ ions have decayed to $\simeq 1/4$ of their initial number of particles, while about half of the initial $^{236}\mathrm{Th}^{88+}$ particles have remained. Consequently, the volume of the two ion clouds is reduced to the point that they don't overlap any more. Therefore their trajectories become separate, resulting in separate frequency peaks in the Schottky spectrum with a $\simeq$ 40 Hz difference. The frequency drifts between subsequent spectra have been corrected in this picture.
The resulting mass resolving power R for a mass difference $\Delta m = 19$ Hz = 435 keV as expressed by the FWHM of the $^{236}\mathrm{Th}^{88+}$ peak is

$$R = \frac{m}{\Delta m} \simeq 5 \cdot 10^5 \tag{4.8}$$

The resolving power achieved in the present study is similar to that of previous Schottky mass measurements [21], [27], [39].

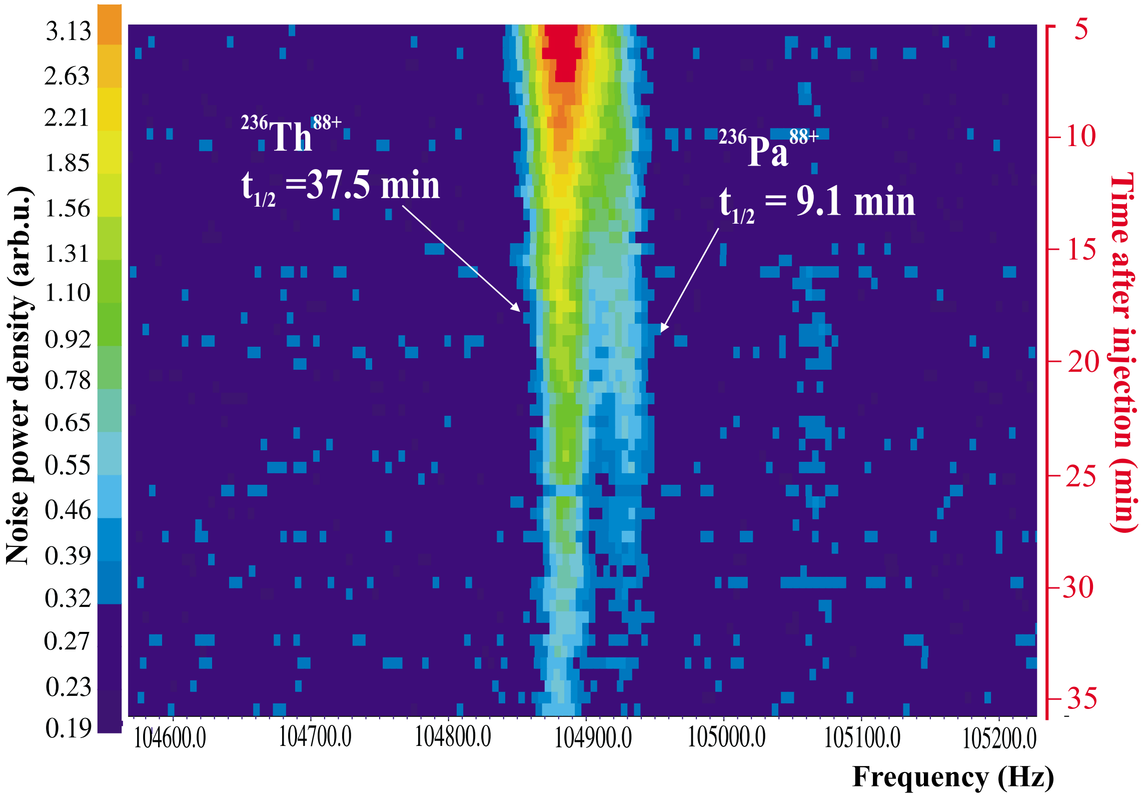

Figure 4.9: A waterfall diagram exhibiting the separation of a $^{236}\mathrm{Pa}^{88+}$ peak from a $^{236}\mathrm{Th}^{88+}$ peak when their number of particles is decreased.

4.2.1 Peak identification

The procedure of identifying the frequency peaks of every spectrum, i.e. finding out which nuclide each represents, was carried out by applying an algorithm based on eq. 2.7 to the possible candidate nuclei. The candidates were selected by the following criteria:

- production cross-sections $\sigma \geq 1\ \mu b$, calculated by the EPAX2 code [8]. Since charge-exchange and nucleon pick-up reactions are possible in addition to projectile fragmentation, we considered nuclei with $75 \leq Z \leq 93$.

- FRS transmission, ESR injection and storage, as explained in 2.1.2. The cooler velocity β_{cooler}, acquired by all the ions as β_{ion}, depends on the effective electron cooler voltage $V_{c,eff}$ of every setting according to

  $$\beta_{cooler} = \beta_{ion} = \sqrt{1 - \frac{1}{\left(1 + \frac{eV_{c,eff}}{m_e c^2}\right)^2}} \tag{4.9}$$

  where e, m_e and c are the electron charge, electron mass and the speed of light, respectively. $V_{c,eff}$ is the applied electron cooler voltage V_c corrected for the space-charge potential due to the cooler current I_c [40] and is given by

  $$V_{c,eff} = V_c - \frac{113 \cdot I_c}{\beta_{cooler}} \tag{4.10}$$

- half-life $t_{1/2} \geq 1$ s, since this is the minimum time required for electron cooling.

- charge states ranging from having 0 to 4 electrons, since the Be-like ions also have considerable transmission yields (see Fig. 2.2).

The applied identification algorithm was the following: Initially, a peak of frequency f_i with specific characteristics, such as an estimable half-life or a very high intensity, was assigned to a candidate nuclide with similar characteristics and a mass-to-charge ratio $(m/q)_i$. A neighboring peak of frequency f_j, $2\ kHz \leq f_i - f_j \leq 40\ kHz$, was attributed to another candidate with $(m/q)_j$ according to eq. 2.7, considering the α_p factor known. Then the $(m/q)_k$ of another peak of frequency f_k was correlated to the acquired $(m/q)_j$ by eq. 2.7, and so forth. In case that more than one candidates satisfied eq. 2.7 at each step, we chose the candidate with the following properties:

- literature half-life closest to the observed one

- peak intensity complying with the candidate's production and transmission yield in the simulated spectra for this specific setting

- probability to be produced by decays or reactions of the expected nuclei of this setting.

After several such steps the α_p was calculated from eq. 2.7 using the deduced mass-to-charge ratios of all the possible pairs of frequencies with a difference Δf in a range $2\ kHz \leq \Delta f \leq 40\ kHz$ and plotted in comparison to the expected curve. Inside the above Δf range, α_p should vary smoothly with orbit length. Large deviations from the expected values and discontinuities of the α_p curve were assumed to be caused by misidentifications and the corresponding peaks were assigned to a different probable candidate. The whole procedure was iterated until the selected candidates satisfied the above physical conditions while producing a smooth α_p curve with a plausible form.

In order to calibrate the α_p factor for our experimental conditions, the on-line monitored frequency values of a selected peak were noted for different values of the cooler voltage. The obtained α_p points were scattered around a mean value of 0.18 with a deviation of 0.015. Thus the needed fine structure of the

α_p curve could not be deduced. The reason of this scattering was later found to be a 1 V and 1 mA uncertainty in the readout of the cooler voltage V_c and current I_c, respectively. Such variations were calculated to cause a change $\delta\alpha_p$ up to $9 \cdot 10^{-3}$, thus blurring the form of the α_p factor. Therefore, we assumed a form of the α_p curve similar to that of the previous experiment, since different ion-optical settings at that time scarcely affected the curve's shape [22], (see Fig.4.10). For the mean pathlength of every studied pair of nuclides, we allowed for a 0.02 variation around the mean α_p value of the two magnet settings of 1997 for this pathlength. The α_p values acquired after identifying the spectra of our experiment are plotted in Fig.4.10 along with those of the 1997 SMS experiment. It can be seen that the shape of the momentum compaction factor is basically preserved in all three cases.

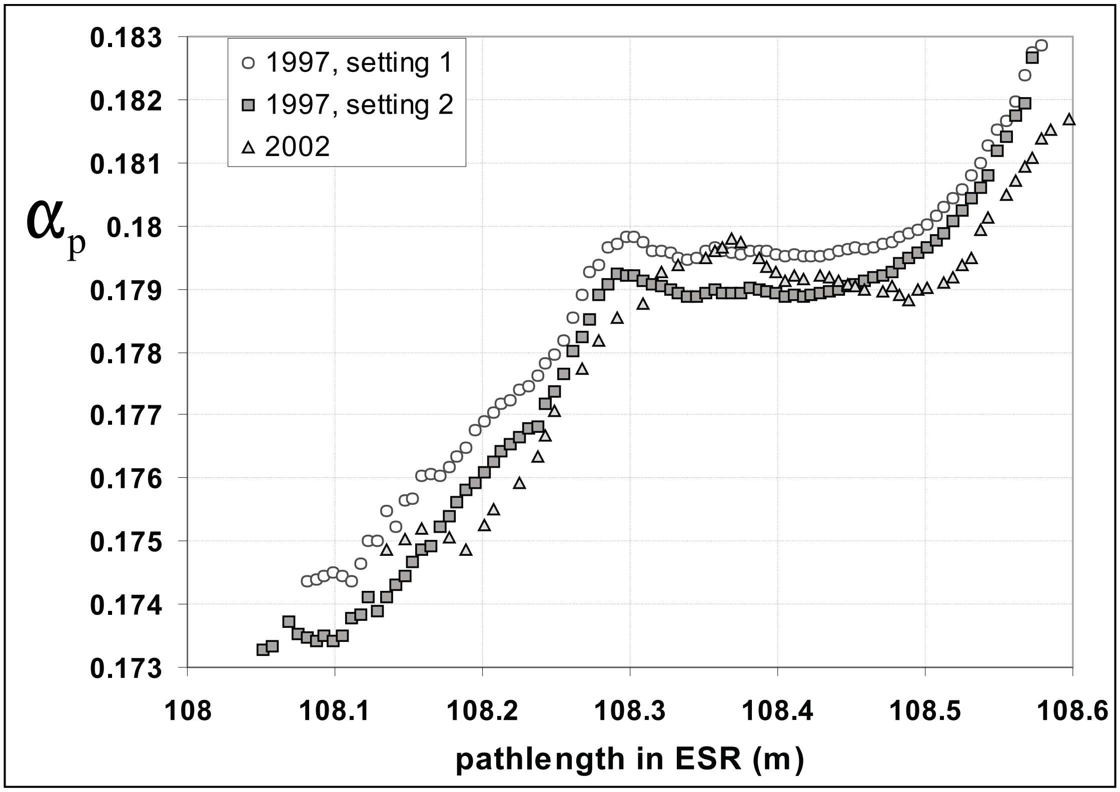

Figure 4.10: Momentum compaction factor α_p as a function of pathlength in the ESR, averaged over all analyzed injections of every displayed ion-optical settings.

A typical Schottky spectrum of the analyzed data contained at best no more than 40 real frequency peaks. This low amount of ion signatures in the spectra is caused from the high background offset of our spectra. Injections with settings by which sections of their spectra overlap assert their identification. Injections with very few peaks (≤ 5) were excluded from our analysis since they could not be unambiguously identified due to their poor statistics. Injections lasting ≤ 4 min were not taken into account either, as this time span is not sufficient for estimating the lifetime of the present ions. Fig. 4.11 shows part of an analyzed Schottky spectrum where the spurious peaks and the nuclides of known and unknown mass are separately indicated.

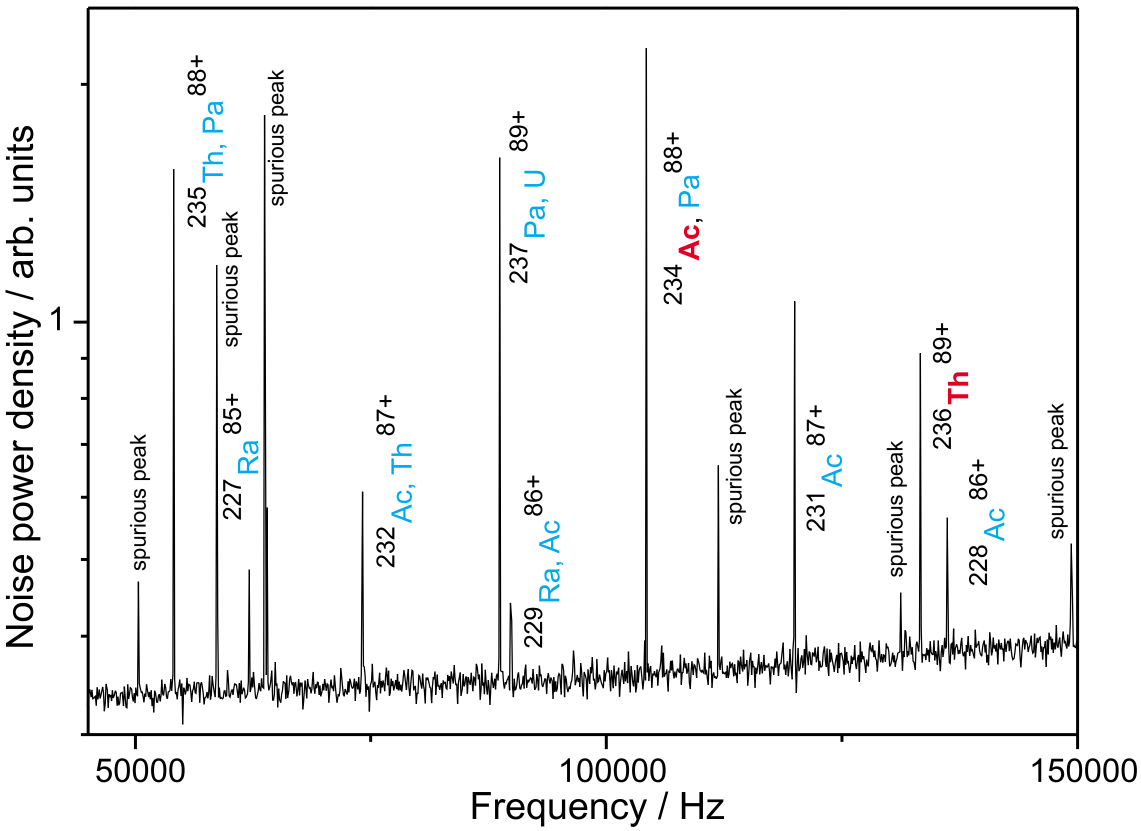

Figure 4.11: Part of a spectrum of an identified injection. Nuclides with previously known mass are labelled in blue while nuclides with masses determined in this study in red color. The indicated doublets are resolved by zooming on them.

4.2.2 Mass determination

The mass analysis was carried out by applying the maximum likelihood method using a correlation matrix [21]: The μ-th frequency peak f_j^μ of the j-th frequency spectrum, attributed to an ion of mass m_j^μ and charge q_j^μ, is considered to be correlated to the other peaks in this spectrum by a polynomial $\sum_k a_j^k (f_j^\mu)^k$ of degree k and coefficients a_j^k :

$$\frac{m_j^\mu}{q_j^\mu} - \sum_k a_j^k (f_j^\mu)^k = l_j^\mu \pm \Delta_j^\mu \tag{4.11}$$

The value l_j^μ is the deviation of the mass-to-charge ratio m_j^μ / q_j^μ from the polynomial fit and has a Gaussian distribution with standard deviation Δ_j^μ around 0 [21]. Δ_j^μ is proportional to the standard deviation of the frequency peak $\sigma_{f_j^\mu}$. The number of different masses m_j^μ in eq. 4.11 is reduced by transforming the mass value of nuclides with several electrons to the mass value of the same nuclides in a fully ionized state. In this way the same isotope can be present in different frequency spectra, interconnecting them via the system of equations 4.11. For the transformation purposes the electron rest masses and their binding energies were subtracted from the mass values. The binding energies of the K1 and K2 electrons were calculated according to [41] and [42], while those of the L1 and L2 electrons according to

$$E = 0.25 \cdot m_e \cdot \left(1 - \sqrt{1 - (Z_{eff} \cdot \alpha)^2}\right) \ , \tag{4.12}$$

where the effective atomic number due to the screening effect is $Z_{eff} = Z - 0.36$ for the L1 electron, $Z_{eff} = Z - 0.89$ for the L2 electron and $\alpha = \frac{1}{137}$ is the Rydberg constant [43].
Additional equations, relating each of the η reference masses of bare nuclei present in our analysis m_η to the literature value of these masses m_η^c, reads

$$m_\eta - m_\eta^c = l_\eta \pm \Delta m_\eta \ , \tag{4.13}$$

where the difference of these masses l_η has a 0 mean value and a standard deviation Δm_η that is equal to the uncertainty of m_η^c.
The mass values m_η are obtained by applying the maximum likelihood method which aims at maximizing the joint probability density function L:

$$L = L_c \cdot L_{exp} = \prod_\eta G(l_\eta, \Delta m_\eta) \cdot \prod_{j,\mu} G(l_j^\mu, \Delta_j^\mu) \ . \tag{4.14}$$

L_c denotes the calibration term while L_{exp} the experimental term of the function L. Both terms are expressed by Gaussian distributions $G(l, \sigma)$. Solving the equations corresponding to the maximum L [22], [21], provides the mass values m_η through a correlation matrix $\mathbf{W}$ of dimensions $N_n \times N_n$, where n denotes the number of different nuclides, according to the expression

$$\mathbf{W}\vec{M} = \vec{w} \ . \tag{4.15}$$

The vector $\vec{w}$ depends on the reference masses and their electron binding energies. The components of the vector $\vec{M}$ were obtained by an iterative procedure aimed at its convergence [22], [21]. The statistical error $\sigma_{m_\mu}^{stat}$ of the derived masses m_μ, including the uncertainties of the reference masses and of the frequency determination, was obtained from the diagonal elements of the inverse matrix $\mathbf{W}^{-1}$:

$$\left(\sigma_{m_\mu}^{stat}\right)^2 = \mathbf{W}^{-1}{}_{\mu\mu} \tag{4.16}$$

The above described method was applied on the unambiguously identified injections of the experiment, which belonged to one specific cut. Disturbed frequency lines caused by mixtures of ions with neighboring m/q were not taken into account. Very broad lines ($\geq$ 40 Hz) neither. A polynomial fit of 4th order was applied for the whole spectrum. The values of the already measured masses used for the mass evaluation were taken from [44]. The nuclides used as references to calibrate the analyzed spectra were carefully selected out of all these measured known masses and are listed in Table 4.1. The selection criteria were such that their mass value should be measured by two or more different experimental techniques and that these measurements should agree with each other. The uncertainty of the reference masses was limited to 30 keV.

4.3 Estimation of systematic error

In order to estimate the systematic error of our measurements each reference mass m_η of Table 4.1 was redetermined assuming that its mass is unknown. The

Table 4.1: Reference masses used for the calibration of Schottky frequency spectra. The mass number (A), proton number (Z) and element name (El.) are given in the first three columns. The mass excess (ME) with corresponding errors (σ_{ME}) are given in the fourth and fifth columns, respectively. The displayed values are taken from Ref. [44].

A	Z	El.	ME keV	σ_{ME} keV
225	87	Fr	23810	30
227	88	Ra	27179.0	2.4
230	88	Ra	34518	12
231	90	Th	33817.3	1.8
232	90	Th	35448.3	2.0
233	90	Th	38733.2	2.0
235	92	U	40920.5	1.8
236	92	U	42446.3	1.8
237	92	U	45391.9	1.9
238	92	U	47308.9	1.9

deviation of their recalculated mass values $\widetilde{m}_\eta$ from their literature values (see Table 4.1) are summarized in the Table 4.2. The systematic error (σ_m^{syst}) of the

Table 4.2: Deviations of the reference mass values obtained from our mass calibration by assuming each mass is unknown, from the literature values of Table 4.1. The mass number (A), proton number (Z) and element name (El.) are given in the first three columns. The deviation from the literature value (Δ_m) and its uncertainty are given in the fourth and fifth column, respectively. $\sigma_{m_\eta}^{stat}$ denotes the mass uncertainty of every reference mass m_η as obtained in our analysis and σ_{m_η} represents the uncertainty of its literature value.

A	Z	El.	Δ_m keV	$\sqrt{(\sigma_{m_n}^{stat})^2 + \sigma_{m_\eta}^2}$ keV
225	87	Fr	-35	30
227	88	Ra	+75	5
230	88	Ra	-237	13
231	90	Th	+259	6
232	90	Th	+327	4
233	90	Th	+266	4
235	92	U	-1	6
236	92	U	+59	14
237	92	U	-510	5
238	92	U	-180	4

measurement was then determined from the relation:

$$\sum_{\eta} \frac{\left(m_{\eta} - \widetilde{m}_{\eta}\right)^{2}}{\left(\sigma_{m_{\eta}}\right)^{2} + (\sigma_{m}^{syst})^{2} + (\sigma_{m_{\eta}}^{stat})^{2}} = N_{ref}, \tag{4.17}$$

where $N_{ref} = 10$ is the number of the reference masses used. The obtained systematic error amounts to 243 μamu or 226 keV and was quadratically added to the errors of the measured masses. The acquired systematic error is about 10 times larger than in the previous ESR Schottky mass measurement [22], since the new data acquisition system was not perfectly optimized in our experiment, thus providing spectra with high background, as was explained in detail in section 4.1.4. The resulting low amount of peaks in the acquired frequency spectra leads to a low number of correlations in the applied matrix analysis. Therefore the evaluation system is very sensitive to removing anyone of the reference masses for recalculating it, yielding a high deviation from its literature value (see Table 4.2).

Chapter 5

Results

An overview of the mass surface covered by the present work is presented in Fig. 5.1. In total 28 different nuclides were observed in the analyzed frequency spectra, 10 of which were used for calibration purposes (see Table 4.1). 5 nuclides were not considered in the mass analysis, as contaminations from other nuclear species with similar m/q values could not be excluded. The mass values of three nuclides were experimentally obtained for the first time in the frame of this work and are listed in Table 5.1. The deviation of previously known masses not used in the frequency calibration from their literature values [44] is shown in Fig. 5.2, which makes evident that these masses are reproduced well in our analysis. The deviations can be characterized by the reduced χ^2 which is defined as:

$$\chi^2 = \frac{1}{n} \sum_{i=1}^{n} \frac{(m_{i,1} - m_{i,2})^2}{\sigma_{i,1}^2 + \sigma_{i,2}^2},$$

where n is the number of the compared values. $m_{i,1}$, $\sigma_{i,1}$ and $m_{i,2}$, $\sigma_{i,2}$ are the mass values and their uncertainties of two different measurements (1 and 2). A χ^2 value of 0.76 was obtained from the comparison of 10 masses, serving as an independent check that the obtained systematic uncertainty is an upper limit of the uncertainty of our measurement.

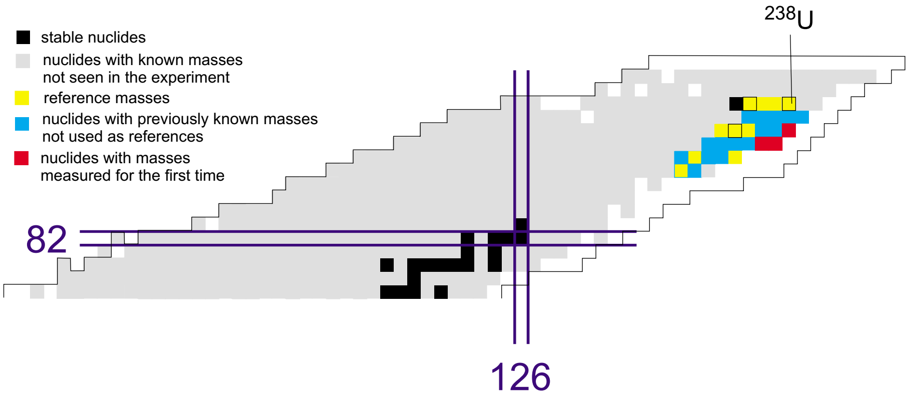

■ stable nuclides
nuclides with known masses not seen in the experiment
reference masses
nuclides with previously known masses not used as references
nuclides with masses measured for the first time
238U
82
126

Figure 5.1: Part of the chart of nuclides with indicated masses measured in this work.

Table 5.1: Mass values measured for the first time. The mass number (A), proton number (Z) and element name (El.) are given in the first three columns. The experimental mass excess (ME) of every nucleus and its corresponding error (σ_{ME}) are given in the fourth and fifth columns, respectively. The extrapolation for the mass excess (ME_{AME}) and its uncertainty ($\sigma_{ME_{AME}}$) from Ref. [44] are given in the last two columns.

A	Z	El.	ME keV	σ_{ME} keV	ME_{AME} keV	$\sigma_{ME_{AME}}$ keV
233	89	Ac	41373	226	41500	300
234	89	Ac	44721	226	45100	400
236	90	Th	46305	226	46450	200

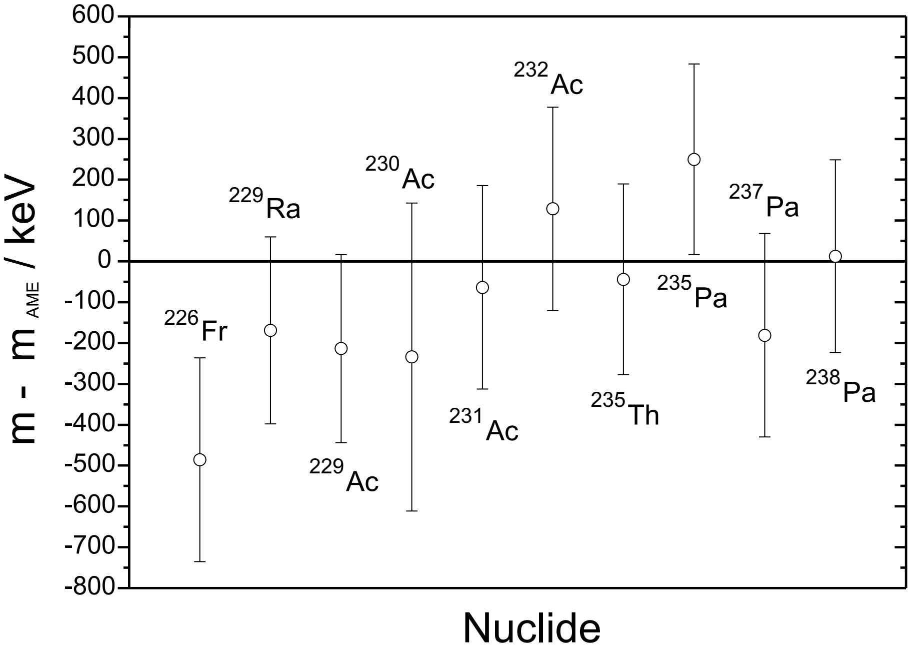

Figure 5.2: Deviation of previously known mass values not used for the calibration purpose to their literature values [44]

5.1 Comparison with theoretical predictions

Although the uncertainties of the newly measured masses are rather high, it is worthwhile comparing them with the predictions of modern mass theories. One of the main motivations for this comparison is that the measured masses belong to neutron-rich nuclides above lead where the experimental information is scarce. Hence a limited number of experimental data is available for testing theoretical models which are also used to predict the properties of very exotic nuclides as e.g. superheavy elements or r-process nuclides.

Nowadays, mass models can be divided in two main categories: The first one, comprising the macroscopic-microscopic models, is based on the well-known Bethe-Weizsäcker formula [45] which represents the liquid-drop model of the nucleus. This macroscopic formula for the mass $m(Z, N)$ of a nucleus with Z protons and

N neutrons reads [1, 46]:

$$c^2 \cdot m_{mac}(Z,N) = c^2 \cdot Z \cdot m_p + c^2 \cdot N \cdot m_n - a_v \cdot A + a_s \cdot A^{2/3} + a_c \cdot Z^2 \cdot A^{-1/3} + a_{as} \cdot \frac{(Z - A/2)^2}{A}, \tag{5.1}$$

where m_p and m_n is the proton and neutron mass, respectively, and A is the mass number of the nucleus. The other parameters are: $a_v = 15.85$ MeV - volume parameter, $a_s = 18.34$ MeV - surface parameter, $a_c = 0.7110$ MeV - Coulomb parameter and $a_{as} = 92.86$ MeV - asymmetry parameter [46]. The surface and Coulomb terms are deformation dependent [47]. The microscopic parts added to the above formula are the shell correction energy and the pairing correlation energy [47]. The shell correction is calculated using the method proposed by V.M. Strutinski [48] and the pairing can be treated with Bardeen-Cooper-Schrieffer [49] or Bogoliubov-Valatin theory [50]. There is a wide range of macroscopic-microscopic models developed in the past. For the present comparison the Finite-Range Droplet Model (FRDM) and Finite-Range Liquid Drop Model (FRLDM) will be adopted.

The purely microscopic mass theories are based on the not precisely known interactions between nucleons. The main idea in studying the atomic nucleus is that all the nucleons move independently in some effective potential (mean field models). In non-relativistic theories the nucleus is calculated self-consistently using the Hartree-Fock method with effective forces of Skyrme (zero-range) or Gogny (finite-range). Gogny calculations require large computing power and are not yet tabulated in the literature for any of the developed effective force. The Skyrme calculations profit from the simpler delta-interactions and a variety of

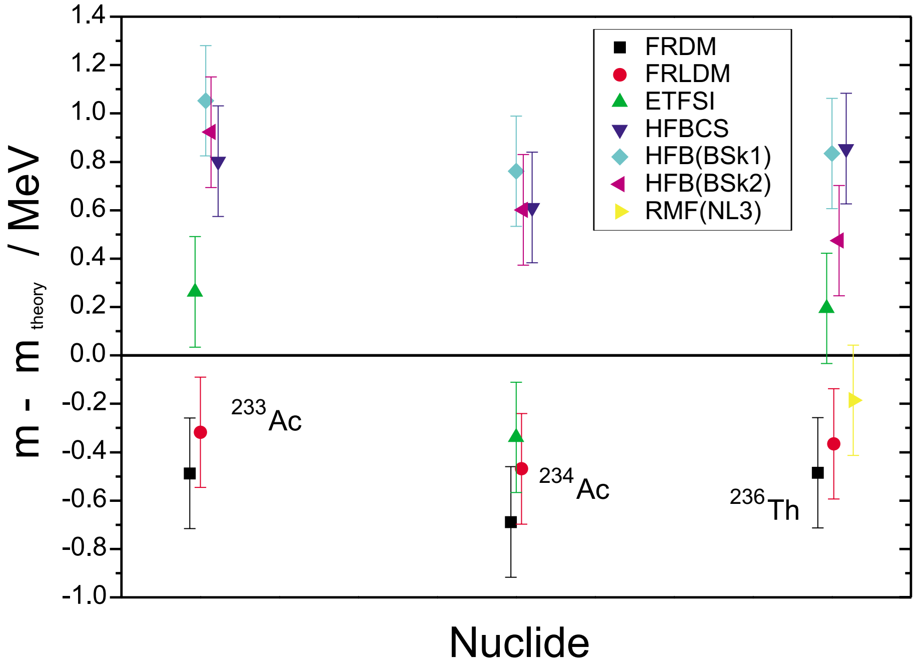

Figure 5.3: Comparison of the new mass values with selected theories described in the text. Their abbreviations are given in the legend and the theoretical predictions are referred to in the text.

Table 5.2: Predictive power of different mass models. The names of the model and the corresponding references are given in the first column. The calculated values of σ_{rms} and σ_{th} are given in the second and third columns, respectively. The fourth column holds the numbers of the compared mass values.

mass model	σ_{rms} [keV]	σ_{th} [keV]	n
macroscopic-microscopic			
Goriely et al.(ETFSI2) [54]	271	147	3
Möller et al.(FRDM) [57]	562	513	3
Möller et al.(FRLDM) [57]	389	313	3
microscopic			
HF-BCS(MSk7) [51]	763	727	3
HFB(BSk1) [52]	891	861	3
HFB(BSk2) [53]	692	653	3
RMF(NL3) [55]	185	-	1

tables exist for different parameterizations of the interaction. In all these calculations the pairing correlations are treated separately using the BCS or Bogoliubov mechanisms. Hartree-Fock-BCS with MSk7 interaction [51] and Hartree-Fock-Bogoliubov with BSk1 [52] and BSk2 [53] interactions are used in the comparison. The BSk1 and BSk2 differ from each other by the magnitude of the cut-off energy which limits the number of single-particle levels around the Fermi surface taken for the pairing. The Extended Thomas-Fermi plus Strutinski Integral (ETFSI) model [54] is as well taken for the comparison, which is an intermediate theory between purely microscopic and macroscopic-microscopic models.

The relativistic mean field (RMF) theory is a fast developing theory which treats all the nucleons relativistically by solving the Dirac equation. The interaction is mediated by three virtual mesons. The only tabulated RMF calculations with the NL3 parameters set and BCS pairing treatment presently exists for even-even nuclides [55].

The comparison of the newly measured masses of this work to some selected theories is illustrated in Fig. 5.3.

The *rms* deviation (σ_{rms}) characterizes the predictive power of a model [56] and is defined as :

$$\sigma_{rms}^2 = \frac{1}{n}\sum_{i=1}^{n}(m(exp) - m(theory))_i^2, \tag{5.2}$$

where n is the number of compared experimental ($m(exp)$) and theoretical ($m(theory)$) masses. A criterion accounting for the experimental uncertainties is [57, 58]:

$$\sum_{i=1}^{n}\frac{(m(exp) - m(theory))_i^2}{(\sigma_{exp})_i^2 + \sigma_{th}^2} = n, \tag{5.3}$$

where $(\sigma_{exp})_i$ is the experimental error for each experimental mass value i and σ_{th} is the error which has to be added to obtain a reduced χ^2 value of 1. The σ_{rms} and σ_{th} were calculated for the selected mass models and the results are summarized in Table 5.2. It is clearly seen from this table that only two models, namely the RMF(NL3) [55] and ETFSI2 [54], agree with the new experimental data.

5.2 Half-life measurement

Besides determining the mass of observed nuclei, time-resolved Schottky mass spectrometry offers the possibility to measure their half-lives, too. An example of half-life estimation is displayed on Fig. 5.4: On the upper part the decay of ^{233}Ac^{88+} nuclei becomes obvious from the decrease of its peak intensity with time, in contrast to the neighboring much longer-lived ^{233}Th^{88+} peak. The lower part of the figure shows the deduced exponential decay curve of ^{233}Ac^{88+}. Its half-life $t_{1/2}$ is obtained from its exponential decay constant $\lambda = (4.85 \pm 0.41) \cdot 10^{-3}\ s^{-1}$ and its Lorentz factor $\gamma = 1.376749$, by taking into account a correction for the ring losses, according to the relation:

$$t_{1/2} = \frac{ln2}{\gamma\lambda - \gamma_r\lambda_r}\ . \tag{5.4}$$

The ring losses are deduced from the apparent slight intensity decrease of a peak attributed to a stable nucleus. Since a suitable H-like candidate was not present

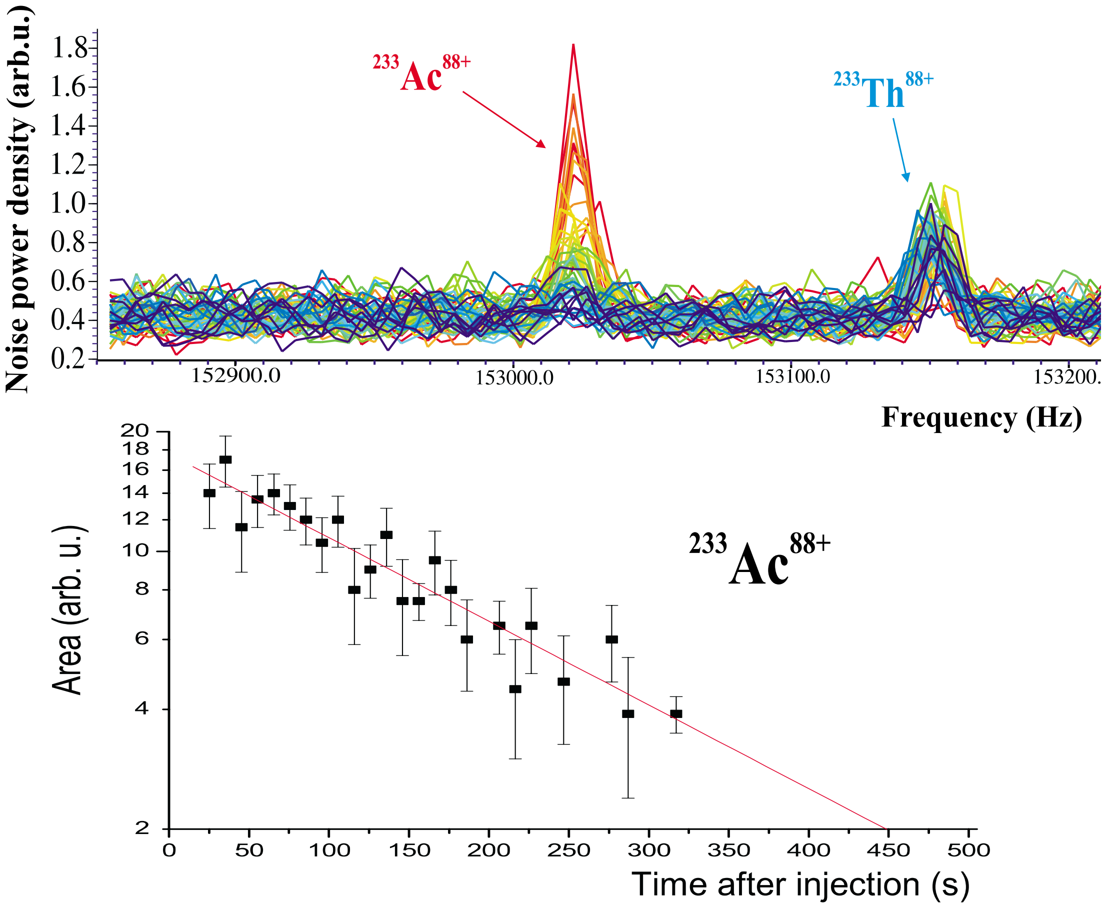

Figure 5.4: Upper part: Subsequent 10 s Schottky spectra of an injection, zoomed on a decaying ^{233}Ac^{88+} nuclide of previously unknown mass and a much more stable ^{233}Th^{88+} nuclide of known mass. Lower part: The deduced decay curve of ^{233}Ac^{88+}. The ordinate is in logarithmic scale.

in the studied cut, a $^{238}U^{88+}$ peak in a setting with $\gamma_r = 1.368528$ was selected for this calculation. An exponential fit to the apparent decay of $^{238}U^{88+}$ yielded the decay constant value due to the ring losses $\lambda_r = (5.062 \pm 0.066) \cdot 10^{-4}\ s^{-1}$. Then the half-life of $^{233}Ac^{88+}$ obtained by eq. 5.4 is:

$$t_{1/2} = (116 \pm 11)\ s\ . \tag{5.5}$$

The obtained value was compared to the literature half-life value for the neutral atom [59], which was adjusted to the H-like atom by calculations based on [60]. These calculations take into account the rates of all the possible β-transitions. The Q-value of the neutral atom β-decay, considering negligible the binding energy of the last electron which is located in the 6d shell and using our new experimental mass value for the ^{233}Ac, is

$$Q = m_{(^{233}Ac)} - m_{(^{233}Th)} = 2640\ keV. \tag{5.6}$$

Using this Q-value and the known decay scheme of neutral ^{233}Ac [59], we obtained the half-life for the H-like charge state of ^{233}Ac as

$$t_{(1/2)rec} = (138 \pm 10)\ s\ . \tag{5.7}$$

Comparing the results of equations 5.5 and 5.7 one sees that they agree within 2 σ, which is very satisfactory, considering that this experiment was not aiming at half-life determinations. This result displays the potential of Schottky mass spectrometry for half-life measurements, which was fully exploited in the following experiment, dedicated at measuring the half-life of $^{207}Tl^{81+}$.

The daughter nucleus $^{233}Th^{89+}$ of the studied β^- decay of $^{233}Ac^{88+}$ is not observed at the expected frequency 271500 Hz for the present settings of $V_{cooler} = 192600$ V, $I_{cooler} = 497$ mA and LO = 58.75 MHz. A plausible reason for not observing the daughter nucleus is that the background offset is higher than the level of a few particles, thus covering the newly produced $^{233}Th^{89+}$ particles. In this case, definite conclusions about the number of particles that correspond to a specific peak area cannot be reached.

As a further very important improvement for future experiments, a comparison between spectra averaged over the same amount of blocks but with a different starting block can lead to an estimation of the cooling time needed for every ion after injection into the ESR. The study of ions with half-lives in the order of a second could be then optimized by analyzing spectra starting exactly after the ion of interest is cooled [35].

Bibliography

[1] A. Bohr, B.R. Mottelson, *Nuclear Structure*, World Scientific Publ., Singapore, 1998.

[2] D. Lunney et al., Rev. Mod. Phys. **A75**, 1021 (2003).

[3] L. Groening and W. Barth, *Measurements and Simulations on the Beam Brilliance in the Universal Linear Accelerator UNILAC at GSI*, http://linac2002.postech.ac.kr/db/proceeding/TU419.PDF

[4] *Commissioning of IH-RFQ and IH-DTL for the GSI high current LINAC*, http://arxiv.org/ftp/physics/papers/0008/0008136.pdf

[5] J.-J. Gaimard and K.-H. Schmidt, Nucl. Phys. **A531**, 709 (1991).

[6] H. Geissel et al., Nucl. Instr. and Meth. in Phys. Res. **B70**, 286 (1992).

[7] H. Geissel et al., Ann. Rev. Nucl. and Part. Sci. **45**, 163 (1995).

[8] K. Sümmerer, B. Blank, Phys. Rev. **C61**, 034607 (2000).

[9] C. Scheidenberger, H. Geissel, Nucl. Instr. and Meth. in Phys. Res. **B135**, 25 (1998).

[10] C. Scheidenberger at al., Nucl. Instr. and Meth. in Phys. Res. **B142**, 441 (1998).

[11] N. Iwasa et al., Nucl. Instr. and Meth. in Phys. Res. **B126**, 284 (1997).

[12] D. Bazin et al., Nucl. Instr. and Meth. in Phys. Res. **A482**, 307 (2002).

[13] M. Hausmannn et al., Nucl. Instr. and Meth. in Phys. Res. **A446**, 569 (2000).

[14] J. Stadlmann, *Erste isochrone Massenmessung kurzlebiger Nuklide am Experimentierspeicherring der GSI*, PhD Thesis, Justus-Liebig Universität Giessen (2002).

[15] T. Winkler et al., Nucl. Instr. and Meth. in Phys. Res. **A391**, 12 (1997).

[16] M. Steck et al., Phys. Rev. Lett. **77**, 3803 (1996).

[17] D. Möhl et al., Phys. Rep. **58**, 76 (1980).

[18] F. Nolden et al., Nucl. Instr. and Meth. in Phys. Res. **A441**, 219 (2000).

[19] D. Boutin et al., GSI Scientific Report 2003, 18 (2003).

[20] J. Borer et al., Proc. IXth Conf. on High Energy Accelerators, 53 (1974)

[21] T. Radon et al., Nucl. Phys. **A677**, 75 (2000).

[22] Y.A. Litvinov, *Basic Nuclear Properties of Neutron-Deficient Nuclei investigated via High Precision Mass Measurements in the Element Range of* $36 \leq Z \leq 92$, Dissertation, Universität Gießen (2003).

[23] 3066 & 3086 3 GHz Real Time Spectrum Analyzer User Manual.

[24] B. Schlitt, *Schottky Mass Spectrometry at the Heavy Ion Storage Ring ESR*, Dissertation, Universität Heidelberg (1997).

[25] S.W. Smith, *The Scientist and Engineer's Guide to Digital Signal Processing*, California Technical Publishing (1997).

[26] U. Schaaf, *Schottky-Diagnose und BTF-Messungen an Gekühlten Strahlen im Schwerionenspeicherring ESR*, PhD Thesis, Universität Frankfurt, (1991).

[27] M. Falch, *Schottky Massenmessungen mit TCAP Datenaufnamesystem am Experimentierspeicherring der GSI*, Dissertation, Ludwig-Maximilians Universität München (2001).

[28] http://www-linux.gsi.de/∼e036/tcap.html (2002).

[29] HP E1430A VXI ADC Operator's Guide (1993).

[30] bc635VME/bc350VXI Time and Frequency Processor, User's Guide, (2000).

[31] HP E1458A 96-Channel Digital I/O Module, User's Manual and SCPI Programming Guide.

[32] C.A.E.N Technical Information Manual, Version 1.0, MOD. V 260, (1999).

[33] Numerical Recipes IN FORTRAN 77: THE ART OF SCIENTIFIC COMPUTING, Cambridge University Press, (1992).

[34] HP E1430A VXI ADC Software Support Reference (1993).

[35] C. Kozhuharov, Private communications.

[36] T. Radon, *Massesnmessung neutronenarmer Wismutfragmente am Experimentierspeicherring der GSI*, PhD Thesis, Justus-Liebig Universität Giessen (1998).

[37] R.W. Hasse, Phys. Rev. Lett. **83**, 3430 (1999).

[38] R.W. Hasse, Phys. Rev. Lett. **86**, 3028 (2001).

[39] H. Geissel at al., Nucl. Phys. **A685**, 115c (2001).

[40] T. Winkler, *Untersuchungen zur Elektronenkühlung hochgeladener schwerer Ionen*, PhD Thesis, Ruprecht-Karls-Universität Heidelberg (1996).

[41] W.R. Johnson, G. Soff, At. Data Nucl. Data Tables **33**, 405 (1985).

[42] D.R. Plante et al., Phys. Rev. **A49**, 3519 (1994).

[43] J.C. Slater, Phys. Rev. **36**, 571 (1930).

[44] G. Audi et al., Nucl. Phys. **A729**, 3 (2003).

[45] C.F. von Weizsäcker, Z. Phys. **96**, 431 (1935).

[46] A.H. Wapstra, *Handbuch der Physik*, Vol. 38, 1958.

[47] P. Möller et al., At. Data Nucl. Data Tables **59**, 185 (1995).

[48] V.M. Strutinski, Nucl. Phys. **A95**, 420 (1967); Nucl. Phys. **A122**, 1 (1968).

[49] J. Bardeen, L.N. Cooper, J.R. Schrieffer, Phys. Rev. **108**, 1175 (1957).

[50] J.G. Valatin, Phys. Rev. **122**, 1012 (1961).

[51] S. Goriely et al., At. Data Nucl. Data Tables **77**, 311 (2001).

[52] M. Samyn et al., Nucl. Phys. **A700**, 142 (2002).

[53] S. Goriely et al., Phys. Rev. **C66**, 024326 (2002).

[54] Y. Aboussir et al., Nucl. Phys. **A549**, 155 (1992).

[55] G.A. Lalazissis et al., At. Data Nucl. Data Tables **71**, 1 (1999).

[56] P.E. Haustein, At. Data Nucl. Data Tables **39**, 185 (1988).

[57] P. Möller et al., At. Data Nucl. Data Tables **59**, 185 (1995).

[58] T. Radon et al., GSI Report **2001-06**, 1 (2001).

[59] K.L. Gippert et al., Nucl. Phys. **A453**, 1 (1986).

[60] K. Takahashi and K. Yokoi, Nucl. Phys. **A404**, 578 (1983).

Acknowledgements

At this point I would like to thank all the people who helped me throughout my stay at GSI. I am thankful to Prof. Dr. G. Münzenberg for offering me the chance to work in GSI and his interest on my progress. I thank Prof. Dr. Hans Geissel for supervising my work and for showing me what the world of modern physics is like.

I am really grateful to Dr. C. Kozhuharov for his remarks and for all the interesting and educative discussions that we had. I have enjoyed the guidance of Dr. C. Scheidenberger and the friendly office atmosphere that he created. I have appreciated the advices of Prof. Dr. Y. Novikov and Dr. Z. Patyk and all that I have learned from Dr. T. Radon, Dr. J. Stadlmann and Dr. M. Portillo. Special thanks to Dr. Y. Litvinov for the knowledge that he did share with me and for fuelling the final sprint.

I owe many thanks to all the members of the group who were really willing to help me, especially D. Boutin. Last but not least, I thank K. Dermati for all her kind support, especially at adjusting to a new environment.